COPPER INSERTION IN UiO-66 ANALOGUES FOR AMMONIA REMOVAL APPLICATIONS

A Thesis
Presented to
The Academic Faculty

By

Jayraj N. Joshi

In Partial Fulfillment
Of the Requirements for the Degree
Master of Science in the
School of Chemical and Biomolecular Engineering

Georgia Institute of Technology

August 2016

COPPER INSERTION IN UiO-66 ANALOGUES FOR AMMONIA REMOVAL APPLICATIONS

Approved by:

Dr. Krista S. Walton, Advisor
School of Chemical and Biomolecular Engineering
Georgia Institute of Technology

Dr. Ryan P. Lively
School of Chemical and Biomolecular Engineering
Georgia Institute of Technology

Dr. Carson Meredith
School of Chemical and Biomolecular Engineering
Georgia Institute of Technology

Date Approved: 05/12/2016

ACKNOWLEDGEMENTS

I would like to thank first and foremost my academic advisor Dr. Krista Walton, for allowing me to join her research group, even when I was both still struggling with the qualifying exam requirements of the department, and did not have an advisor when many others in my class had already joined research groups and started their graduate work. She gave me a chance to start my research and overcome the hurdles that were preventing me from continuing in graduate school, and I really appreciate this. Dr. Walton has also been very helpful and supportive of my work and progress in my graduate studies, and I look forward to continuing my Ph.D. work as a member of her group.

I would also like to acknowledge all of the current and former members of the Walton Research Group that have assisted me for the duration of the work discussed in this thesis: Bogna, Chris, Cody, Harvey, Mike, Karen, Nick, Michael, Yang, Will, Lalit, Colton, Jake, Julian, Eli, and Yutao. Everyone listed has always been more than willing to lend me a hand with my work, and as a relatively new member of the group, I really appreciate all of their assistance, critique, and guidance. I would also like to acknowledge Ross Verploegh for offering helpful insight on this research.

In particular, I would like to acknowledge former Walton Research Group member Erika Garcia-Gutierrez, whose M.S. thesis work created the foundation for this project. Additionally, I'd like to give a special thanks to Jake Deneff, who was involved in preliminary experiments and related work that was instrumental in the completion of this thesis, as well as Karen Tulig, for her extensive guidance, valuable insight, and willingness to help me on seemingly a daily basis—thank you very much!

Finally, I would like to acknowledge my committee members, Dr. Carson Meredith and Dr. Ryan Lively, for offering their time and insight for this project. Also, I would like to acknowledge the funding sources that facilitated the pursuit of the work discussed here: Army Research Office (ARO) and Defense Threat Reduction Agency (DTRA) contractrs W911NF-10-1-0076.

TABLE OF CONTENTS

LIST OF TABLES

LIST OF FIGURES

ABBREVIATIONS AND SYMBOLS

MOF	Metal–Organic Frameworks
NH_3	Ammonia
H_2O	Water
DMF	N,N-Dimethylformamide
CWA	Chemical Warfare Agent
TIC	Toxic Industrial Chemical
Cu	Copper
$Cu(NO_3)_2$	Copper Nitrate
℃	Degree Celsius
Å	Angstrom
K	Kelvin
RH	Relative Humidity
ppm	Parts per Million
mg	Milligram
mL	Milliliters
m^2	Meter Squared
cm^3	Cubic Centimeter
mmol	Millimole
min	Minute
-ox	Functionalized with Oxalic Acid
-ox-Cu	Functionalized with Oxalic Acid and Copper
-vac	Functionalized with missing linker defects/vacancies

CBRN	Chemical, Biological, Radiological And Nuclear
BTC	1,3,5-Benzenetricarboxylic Acid
BDC	1,2,4-Benzenedicarboxylic Acid
DMA	N,N-Dimethyacetamide
PXRD	Powder X-Ray Diffraction
BET	Brunauer, Emmett, And Teller
ICP-OES	Inductively Coupled Plasma Optical Emission Spectrometry
TG/TGA	Thermogravimetric Analysis
EPR	Electron Paramagnetic Resonance
EXAFS	Extended X-Ray Adsorption Fine Structure

SUMMARY

Development of novel materials for ammonia capture in air filtration devices is of particular importance due to the high availability and toxicity of the gas, but materials currently employed for air purification offer insufficient protection. Characteristics of porosity, stability, and tunability in metal organic frameworks, however, makes this class of nanoporous, crystalline material suitable for enhancing ammonia uptake performance of air purification equipment. Post synthetic modification of UiO-66 type MOFs with copper resulted in the creation of UiO-66-$(COOCu)_2$, whose copper carboxylate functional groups are highly favorable for ammonia chemisorption. Experiments showed UiO-66-$(COOCu)_2$ to possess a high uptake capacity for ammonia, while showing negligible loss in surface area and crystallinity following humid and dry ammonia exposure, and water vapor adsorption experiments. However, the –COOCu moieties were thought to cause significant pore blocking, likely hindering access of ammonia guest molecules into the pore space. Recent studies have shown carboxylic acid functionalities can be incorporated into UiO-66 through missing linker sites, resulting in higher surface area and pore accessibility, while incorporating carboxylic acid functionalities that can be used for copper coordination to enhance ammonia uptake.

This study focuses on the functionalization of defective UiO-66 with copper carboxylate groups, where copper loading and ammonia uptake performance was studied for comparison to other materials used for ammonia adsorption. Furthermore, the kinetic effects of copper loadings on linker and defect site functionalized carboxylic acid groups on UiO-66 were studied, along with their effect on dynamic ammonia capacity.

CHAPTER 1

INTRODUCTION

Researchers have been continuously developing and improving upon air filtration technology and gas masks to defend against toxic industrial chemical (TIC) and chemical warfare agent (CWA) release.[1] The frequent use of sulfur mustard and chlorine gas over a century ago during WWI created a demand for personal breathing protection devices to combat chemical warfare tactics.[2] Current chemical, biological, radiological, and nuclear (CBRN) breathing apparatuses and other air purification devices often contain activated carbon, such as ASZM-TEDA and Calgon BPL, doped with metal salts.[3] Examples of CBRN devices from the U.S. military are provided in Figure 1. Such filters offer protection against many toxic gases, but remain unsuitable for the full range of hazardous chemical agents, particularly low molecular weight, high vapor pressure contaminants.[3,4] In particular, CBRN's are not effective against ammonia, which not only possesses high toxicity and volatility, with an OSHA PEL of 50 ppm and vapor pressure of 7600 mm Hg at ambient temperatures, but is also one of the most abundantly produced commodity chemicals worldwide.[5] Several fatalities following the 2013 ammonium nitrate plant explosion at the West Fertilizer Company in Texas recently revealed the risk of accidental ammonia release, as the plant was located next to a school and other residential areas.[6] Furthermore, precedent for the use of ammonia as a CWA has already been set, as it was used in combination with chlorine in the 2014 chemical attack on Kafr Zita, Syria[7], and an ammonia production facility was previously targeted several times by Serbian forces to provoke NH_3 release during the Yugoslav Wars.[2]

Figure 1. United States military CBRN devices (from left to right: M40, M50, and a concept design). Image taken from Jacoby, M.[1]

Work in the growing field of metal organic frameworks (MOFs) has revealed these novel materials to be possible filtration candidates in the task of ammonia and other TIC/CWA capture applications. MOFs are a class of nanoporous, crystalline materials, comprised of metal oxide clusters coordinated to one another by organic ligands.[8,9] MOFs offer advantages over traditional adsorbents, such as zeolites and carbon based materials, as they have been observed not only to possess high porosities and surface areas, but can also be engineered to contain functional groups offering chemical specificity towards specific adsorbates.[10,11] For instance, a recent review by Jiang et al. showed Brønsted acidity has been engineered in many MOFs, through both their metal centers and linker functional groups, to enhance alkaline gas selectivity, proton conductivity for energy production, and catalytic activity for numerous reactions.[12] Linker functionalities themselves can also be subject to further post synthetic modification through binding other functionalities[13] or cross-linking.[14] These strategies help to enhance ammonia loadings at lower relative pressures[15], making MOFs more relevant for air filtration applications. Several strategies have already been employed to enhance ammonia

selectivity in MOFs, such as acid doping through post synthetic modification[16], and exploiting coordination sites on MOF metal centers, as with the copper based MOF HKUST-1, which has been observed to exhibit strong chemisorption with ammonia on the Cu metal center active sites.[17,18] MOF composites, usually with graphene oxide, have also been investigated for ammonia removal applications, and have been observed to change uptake behavior in both dry and humid conditions. [17,19]

Chemical stability unfortunately limits the practical applicability of MOFs in humid streams, such as the high performing HKUST-1, and ZnBTTB, due to the degradation of metal-linker bonds in the presence of H_2O.[17-20] However, the zirconium based MOF UiO-66 displays negligible loss in BET surface area or crystallinity post water exposure, and also boasts high chemical and thermal stability up to 500 ℃.[21,22] A myriad of linker substitutions have also been functionalized on UiO-66, where –COOH, $–NH_2$, –OH, and other functionalities greatly enhance capacities for ammonia through acid-base interactions and hydrogen bonding.[23] Further post-synthetic modification strategies have used such functionalities to incorporate other groups, as Hou et al. coordinated copper (II) sites to a UiO-66-NH_2 precursor using salicylic acid binding groups.[24] Getman et al. used quantum mechanical calculations to screen several strongly binding metal catechols for improved hydrogen adsorption in several IRMOFs, UiO-68, and UMCM-150.[25] Metal carboxylates offer promising chemical bonding capabilities, where alkali metals were reported to enhance CO_2 capture and selectivity in UiO-66-$(COOH)_2$ by binding the metals to open carboxylic acid sites located on the organic linkers.[26] Copper carboxylate (-COOCu) linker functionalities are of particular interest, as computational studies by Snurr et al. found these groups to possess a high binding energy

(-161.2 kJ mol^{-1}) with ammonia, and the most preferential binding energy favorability with ammonia over water out of the 21 functional groups investigated.[27] Subsequent integration of these functionalities into the MOFs UiO-66-COOH and UiO-66-$(COOH)_2$ by Garcia-Gutierrez led to the creation of two new UiO-66 MOFs, UiO-66-COOCu and UiO-66-$(COOCu)_2$, through post synthetic modification with copper nitrate.[28] Both MOFs retained stability following water exposure, as well as dry and humid ammonia breakthrough experiments, and UiO-66-$(COOCu)_2$ exceeded the project target of 6 mmol NH_3 g^{-1} adsorbent. [28,29]

Accessibility of guest molecules into the frameworks of the two MOFs were said to have been hindered by the bulky copper carboxylate functional groups, predicted from their low surface areas, and it was subsequently hypothesized that most of the adsorption occurred on the surface of the material, leaving the pore space largely underutilized.[28] Therefore, it can be inferred that adding copper carboxylate groups into the MOF framework while maintaining surface area and pore accessibility potentially enhances ammonia adsorption capabilities. Incorporation of linker defects offer a feasible route to accomplishing this, as defects inherently exist in UiO-66 type MOFs.[30] Water adsorption simulations have shown that these defects enhance guest molecule accessibility and hydrophillcity to that of the hypothetical "defect-free" structure.[31] Synthesis modulation, typically through elevating reactant batch acidity, has been employed to increase the amount of missing linker defects in the UiO-66 framework.[32,33] Adding defects experimentally in UiO-66 has not only increased BET surface area, but also facilitated post-synthetic modification and accessibility to the Zr(IV) cluster, as observed by López-Maya et al., where open Zr-O bonds in defective UiO-66 contributed to improved

hydrolytic CWA degradation and lithium alkoxide catalyst incorporation.[34] Pertinent to this study, hydrochloric acid was used create framework defects in UiO-66, averaging 4 out of 12 missing linkers per node[32]. The MOF was then subjected to post synthetic modification with oxalic acid to functionalize carboxylic acid groups into the missing linker defect sites.[33] The resulting material, named UiO-66-ox, yielded increased ammonia uptake through the acid-base interactions of carboxylic acid groups and ammonia, while mitigating the pore blockage phenomenon seen with UiO-66-COOH and UiO-66-$(COOH)_2$, inferred from minimal losses in BET surface area.[33] It is hypothesized that the greater accessible surface area could be maintained for UiO-66-ox after copper functionalization to the carboxyl groups introduced by the oxalic acid species, and will allow for enhanced ammonia sorption among other previously tested UiO-66 type MOFs, while preserving the chemical and thermal stability of the parent MOF, maintaining its practical applicability towards TIC/CWA capture.

The scope of this study is to achieve the following:

1. Develop copper carboxylate functional sites in UiO-66 type analogues
2. Determine kinetic effects of copper loading on UiO-66-$(COOCu)_2$ and UiO-66-ox, which feature carboxyl functionalities in different locations in their respective frameworks
3. Evaluate the ammonia uptake performance of the new MOFs containing copper binding sites under dry and humid conditions

MATERIALS AND EXPERIMENTAL METHODS

2.1 Materials and Synthesis Methods

2.1.1 UiO-66 MOF

UiO-66 is a metal organic framework that has been found to possess high chemical and thermal stability, containing a six-centered zirconium (IV) metal cluster, where the $Zr_6O_4(OH)_4$ octahedra are twelve-coordinated to carboxylic acid groups from terephthalic acid organic linkers.[21] The 3-dimensional, face-centered cubic structure of UiO-66 is comprised of eight tetrahedral cages, with 6 Å triangular windows. [30, 32] A visualization of the UiO-66 structure is provided in Figure 2.

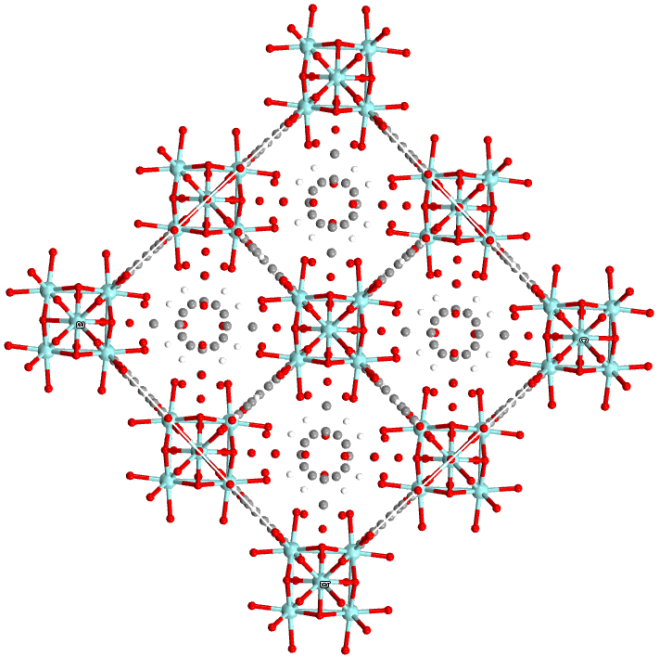

Figure 2. Structure of UiO-66 framework (cyan spheres = Zr, red spheres = oxygen, grey spheres = carbon).

2.1.2 Synthesis Methods

All chemicals used to synthesize MOFs in this study were commercially available and used without further purification. Additionally, all MOF synthesis procedures are based on work in previously published literature. As a visualization aid, the organic linkers used in UiO-66, UiO-66-ox, UiO-66-$(COOH)_2$, and their respective analogues post-metal insertion are provided in Figure 3.

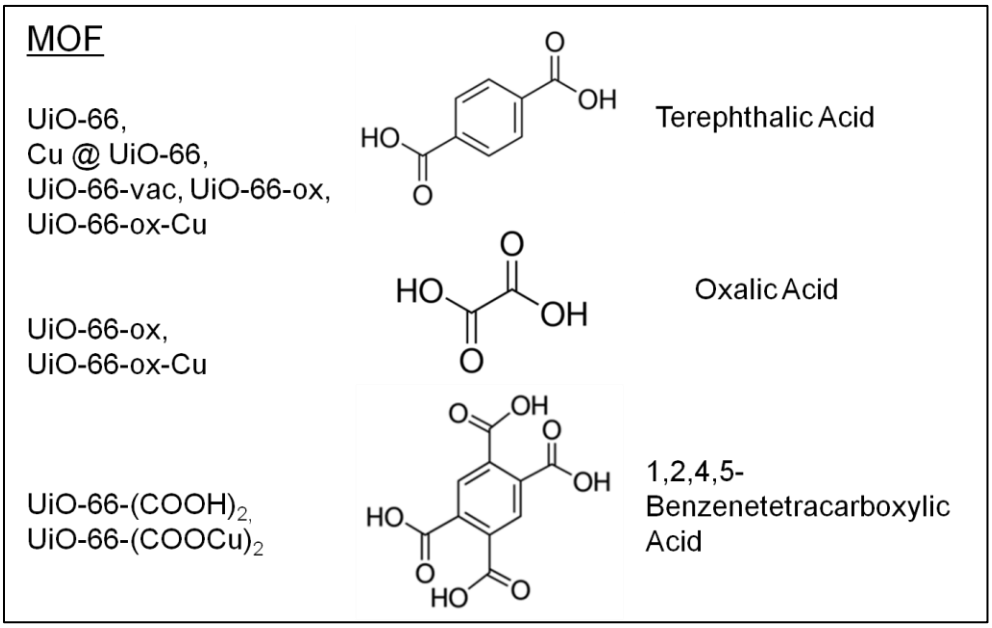

Figure 3. Illustration of organic linkers used for MOFs synthesized in this study.

2.1.2.1 UiO-66

Synthesis of parent UiO-66 was conducted using a scaled-up procedure based on the method used by Cavka et al.[21] An equimolar mixture of zirconium (IV) chloride (0.43 mmol, 100 mg) and terephthalic acid (0.43 mmol, 71.3 mg) were dissolved in 26.5 mL of N,N-dimethylformamide (DMF) in a 60mL glass vial. The solution was then

transferred to an insulated, isothermal oven at 120 ℃ for 24 h. Following the solvothermal synthesis, the resulting solid was filtered and washed three times with DMF, then three times with methanol, and then allowed to dry overnight under ambient conditions. The dried sample was activated under vacuum at 150 ℃ for 24 h.[32]

2.1.2.2 UiO-66-$(COOH)_2$

UiO-66-$(COOH)_2$ was produced to further study UiO-66-$(COOCu)_2$.[28] The synthesis for UiO-66-$(COOH)_2$ was scaled-up from an original route reported in Biswas et al.[35] Furthermore, it should be stated that the order of adding reactants to form UiO-66-$(COOH)_2$ affected the resultant MOF crystallinity in this study, and agitation of the reaction mixture was detrimental to MOF yield and crystallinity, although this was not reported in the original synthesis publication. First, 9 mL of N,N-dimethylacetamide (DMA) and 3.6mL of formic acid were placed in a Teflon lined stainless steel reactor. The addition of 0.38% (v/v) of water was found previously to improve consistency in crystallinity between samples (48 μL of H_2O)[28], and was subsequently placed into the mixture. Equimolar amounts of zirconyl chloride octahydrate (0.93 mmol, 300 mg) and 1,2,4,5-Benzenetetracarboxylic acid (0.93 mmol, 236.4 mg) were then added to the mixture, without stirring. The reactor was then transferred to a programmable oven, where it was heated at a rate of 2.2 ℃ min^{-1} to 150 ℃, and then held constant at that temperature for 24h. The resultant solid was then cooled to room temperature, filtered, and washed three times with DMF, then three times with acetone, and then three times with methanol, and dried overnight under ambient conditions. The as-synthesized sample was activated for 12 h under vacuum at 65 ℃.

2.1.2.3 UiO-66-vac

A UiO-66 analogue with missing linker defects, named UiO-66-vac, was synthesized according to previously published method.[32,33] Figure 4 illustrates the syntheses of UiO-66-vac and UiO-66-ox. Zirconium (IV) chloride (0.54, 125 mg) was placed in a 60 mL glass scintillation vial with 5 mL of DMF. Hydrochloric acid (1 mL) was then added into the glass vial, and the reaction solution was agitated in a sonication bath for 20 minutes. Terephthalic acid (0.75 mmol, 123 mg) was then added to the reaction mixture with 10 mL of DMF, and the solution was agitated again for 20 minutes in a sonication bath. The reactant mixture was then heated in an isothermal oven at 80 ℃ for 24 h. Following the synthesis, the resulting solid was filtered and washed three times with DMF, then three times with ethanol, and then allowed to dry overnight under ambient conditions. The sample was activated under vacuum at 150 ℃ for 24 h.

2.1.2.4 UiO-66-ox

UiO-66-vac was functionalized with carboxyl groups to create UiO-66-ox according to a previous method by DeCoste et al.[33] UiO-66-vac (250 mg) was mixed with ≥99% pure oxalic acid (120 mg) and 10 mL of DMF in a 20 mL glass scintillation vial. The reaction mixture was stirred gently using a magnetic stir bar for 24 h at room temperature. The resulting solid was then filtered and washed three times with DMF, then three times with ethanol, and then was allowed to dry overnight under ambient conditions. The dried sample was activated under vacuum at 150 ℃ for 24 h.

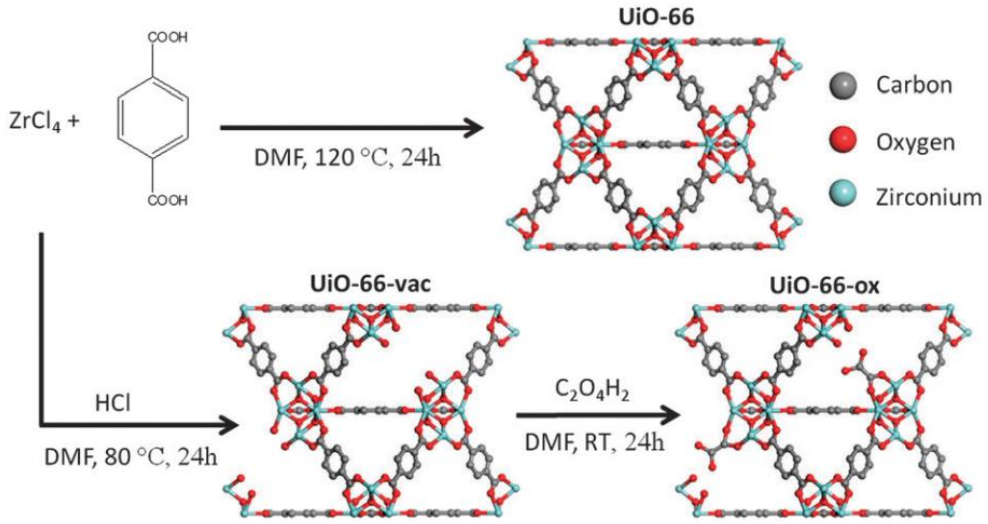

Figure 4. Schematic of UiO-66-vac and UiO-66-ox synthesis routes contrasted with the traditional UiO-66 synthesis route. Replicated from DeCoste et al.[33]

2.1.2.5 Copper Insertion: Cu @ UiO-66, UiO-66-$(COOCu)_2$, and UiO-66-ox-Cu

A reaction procedure to coordinate copper (II) ions to free carboxylic acid groups in UiO-66-ox and UiO-66-$(COOH)_2$ was utilized to synthesize UiO-66-ox-Cu and UiO-66-$(COOCu)_2$, respectively. The metal insertion procedure is based off of a previously used copper coordination procedure for UiO-66-COOH and UiO-66-$(COOH)_2$.[28] The general approach involves mixing the MOF and a metal salt in solution to allow for mass transfer of the target metal into the framework. This methodology has been applied to create Au and Pt impregnations into UiO-66 and UiO-66-NH_2, respectively in previous investigations.[36,37] This approach was also used to impregnate parent UiO-66 with copper to make Cu @ UiO-66 in this study. A visualization of the four copper MOFs is provided in Figure 5, where the metal is hypothesized to exist uncoordinated to the structure in Cu @ UiO-66, and bonded to carboxylic acid functionalities to form copper carboxylate groups in UiO-66-ox-Cu, UiO-66-COOCu, and UiO-66-$(COOCu)_2$.

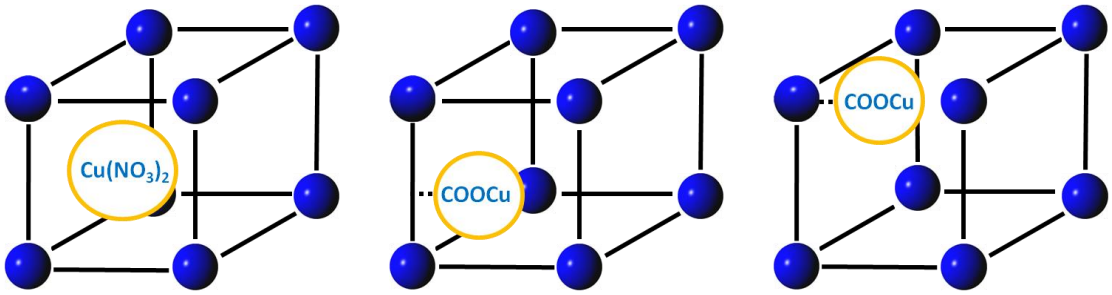

Figure 5. Illustration of predicted copper coordination nature in Cu @ UiO-66 (left), UiO-66-COOCu/UiO-66-$(COOCu)_2$ (middle), and UiO-66-ox-Cu (right). Encircled groups—copper after metal impregnation, blue spheres—zirconium metal center clusters, solid black lines—organic linkers, dotted black lines—chemical bond to functional group.

A 0.1 M solution of copper nitrate trihydrate (99%) in DMF was first prepared in a 60 mL glass scintillation vial, and agitated using a stir plate for at least 30 min to ensure the solution was well mixed. The MOF (UiO-66-ox for UiO-66-ox-Cu, UiO-66-$(COOH)_2$ for UiO-66-$(COOCu)_2$, and UiO-66 for Cu @ UiO-66) was then added to the reaction container in a ratio of 7.6 mg MOF / mL solution (190 mg). The mixture was then transferred to an oil bath set to 65 ℃ and agitated using a magnetic stir bar. The resulting MOF was then filtered and washed three times with DMF, three times with ethanol, and three times with methanol, and then dried overnight under ambient conditions. All MOFs were activated based on the thermal stabilities of their respective parent MOFs, which was shown not to change significantly after metal insertion, where UiO-66-$(COOCu)_2$ was activated at 65 ℃ for 12 h, and 150 ℃ for 24 h for UiO-66-ox-Cu and Cu @ UiO-66, all under vacuum.

2.2 Characterization Techniques

2.2.1 Powder X-Ray Diffraction (PXRD)

Powder X-Ray diffraction patterns of the powder MOF samples were collected using an X'Pert Pro PANanalytical X-ray diffractometer. Measurements were taken at room temperature, with Cu Kα radiation (λ = 1.542 Å), and a step size of 0.02° 2θ, from 4 to 60 degrees. PXRD patterns were compared with both patterns from previous literature and simulated patterns to help verify MOF crystal structures, observe structural integrity following experiments, gauge the impact of adding functional groups on base MOF structures, and study the impact of metal insertion on the diffraction patterns.

2.2.2 Nitrogen Physisorption Isothermal Measurements

Nitrogen adsorption measurements were taken isothermally at 77 K using a Quadrasorb Evo instrument from Quantachrome Instruments. Data from the adsorption measurements were used to calculate the surface area of the materials, by fitting the adsorption data to the Brunauer, Emmett, and Teller (BET) model. The BET model has been suggested by Walton et al. to remain applicable to MOF surface area measurements over a pressure range of 0.005 P / P_0, so a range of $0.005 < P / P_0 < 0.03$ was used in this study.[38] Furthermore, the appropriate BET consistency criteria in accordance with observations of UiO-66 by Gómez-Gualdrón et al. were applied to verify accuracy in surface area measurements.[39] Approximately 30-50 mg of the activated samples were used in generating the isotherms. Activation for samples prior to N_2 physisorption was carried out using a Quantachrome Instruments FloVac Degasser, and activation conditions for the respective samples are detailed in Section 2.1.

2.2.3 Thermogravimetric Analysis (TGA)

Thermogravimetric analysis was used to study the thermal degradation temperatures of synthesized materials, as well as help determine desolvation and dehydration temperatures (used for activation conditions). A Netzsch STA 449 F1 Jupiter instrument was used to collect TGA measurements. Approximately 15-30 mg of sample was placed in a crucible under a 20 mL min^{-1} flow of helium. The samples were then heated from 20-800 ℃ at a rate of 2 ℃ min^{-1}, and then heated isothermally for 2 h at 800 ℃ before terminating data collection.

2.2.4 Inductively Coupled Plasma Optical Emission Spectrometry (ICP-OES)

Elemental analysis using ICP-OES was utilized to determine copper and zirconium metal contents in the samples that were investigated. Data were provided as mass percentages, but are normalized by the calculated theoretical loading of the respective materials (based off of stoichiometry) to negate relative density differences amongst samples. Materials were shipped to ALS Environmental for all ICP-OES measurements.

2.3 Ammonia Breakthrough Measurements

Evaluation of air purification performance was analyzed through breakthrough testing, as this method considers mass transfer limitations, unlike equilibrium measurements, which can greatly impact CBRN performance.[15] Data for dynamic ammonia breakthrough capacities were collected using an in-house built breakthrough apparatus, slightly manipulated from the one described by Mangarella and Walton previously.[40] The schematic is shown in Figure 6. About 5-20 mg of sample was packed

vertically in a quartz tube (4mm ID) to a height of 4.3 mm with porous frits to permit gas flow, resulting in a final volume of 55mm^3. Tubes were also packed with quartz wool prior to breakthrough measurements to avoid pressure drop through the column. Throughout the course of the experiment, the sample in the packed bed was subjected to an inlet ammonia containing stream, until the bed became saturated with the vapor species, after which the gas broke through and was detected by a chemical sensor downstream from the bed. Breakthrough curves were obtained by taking ammonia concentration readings and experiment time readings every 30 seconds. Ammonia concentrations were normalized by activated adsorbent weight, which was measured immediately before breakthrough testing.

Activation was carried out in-situ, using HTS Amptek heat tape in junction with a temperature PID controller, and under 20 mL min^{-1} N_2 flow. Samples were weighed before and after activation to obtain activated weight for dynamic capacity calculations, and were allowed to cool to room temperature under N_2 flow prior to ammonia breakthrough measurements.

Breakthrough measurements were taken in dry and humid conditions at room temperature. Ammonia was introduced to the system at a concentration of 7155 ppm and a flow rate of 4 mL min^{-1}, and mixed with air at a flow rate of 16 mL min^{-1} before entering the packed bed. For wet breakthrough experiments, the air stream passes through a water bubbler, illustrated in Figure 6, before contacting the incoming ammonia. The apparatus under setup for wet breakthrough was observed to result in ~80% RH for wet breakthrough runs, and a calculated NH_3 concentration of 1431 ppm. In dry conditions, the air stream circumvents the bubbler. Ammonia flow was terminated when effluent

concentrations reached 500 ppm to preserve the lifetime of the sensor, and N_2 was flowed in at 20 mL min^{-1} following breakthrough for desorption measurements. Calculated dynamic breakthrough capacities for ammonia have an approximate error of around 10%, as seen with analogous systems.[29,41]

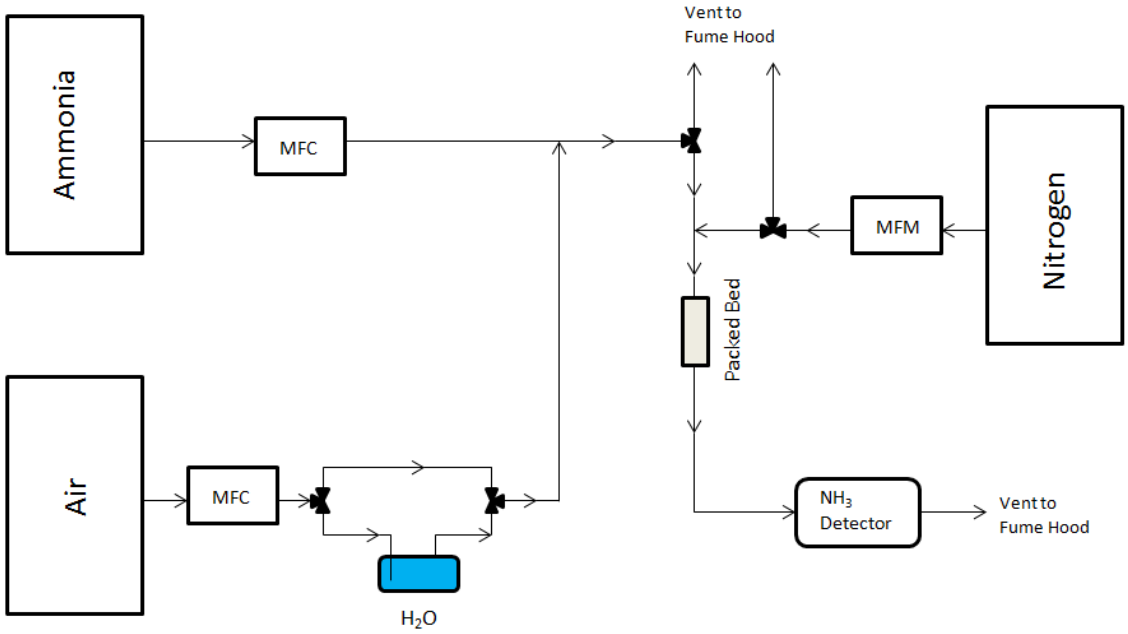

Figure 6. Schematic of ammonia breakthrough system. Pressure gauges immediately upstream and downstream from the packed bed are omitted in this diagram.

2.4 Isothermal Water Vapor Adsorption Measurements

An Intelligent Gravimetric Analyzer (IGA-3) machine was used to collect data for water vapor adsorption experiments. Samples were activated in-situ under vacuum, at their respective activation temperatures, until weight loss (measured continuously) was no longer observed. Data was collected isothermally at 25 ℃ and 1 bar. Samples were exposed to water vapor up to 90% RH to avoid condensation, using a total gas flow rate of 200 mL min^{-1} with dry air as the carrier/balance at each condition.

Results and Discussion

3.1 Materials Synthesis and Characterization

3.1.1 Synthesis and Characterization of MOFs

Four batches of UiO-66-vac were synthesized for this study. The average BET surface areas of the UiO-66-vac samples based on N_2 physisorption measurements were 1516 $\pm$ 83 m^2 g^{-1}, which is consistent with the published experimental value of 1590 m^2 g^{-1} by DeCoste et al.[33] It should be stated that although the surface areas between batches were within standard deviation of measurements and machine error, the location and number of defects in the material are not controlled in the synthesis of UiO-66-vac. Furthermore, simulated surface areas have not been generated for UiO-66-vac or UiO-66-ox, and should be calculated for further study. Elemental analysis in previous literature suggests 4 missing linkers per node correspond to the resultant MOF structure.[32] Subsequently, TG analysis of UiO-66-vac was utilized to verify the reproducibility of the number of missing linker defects for the material used in this work. Figure 7 contrasts the linker loss of UiO-66-vac with parent UiO-66[36], which is assumed to possess non-stoichiometry of 1 out of 12 missing linkers; previously shown to be inherent to the structure. [22,30,31] The activated mass loss of both MOFs in Figure 7 reveals close to 10 % less linker volatilization by mass in UiO-66-vac as observed with UiO-66, in agreement with observable mass loss in the original synthesis via TGA.[32]

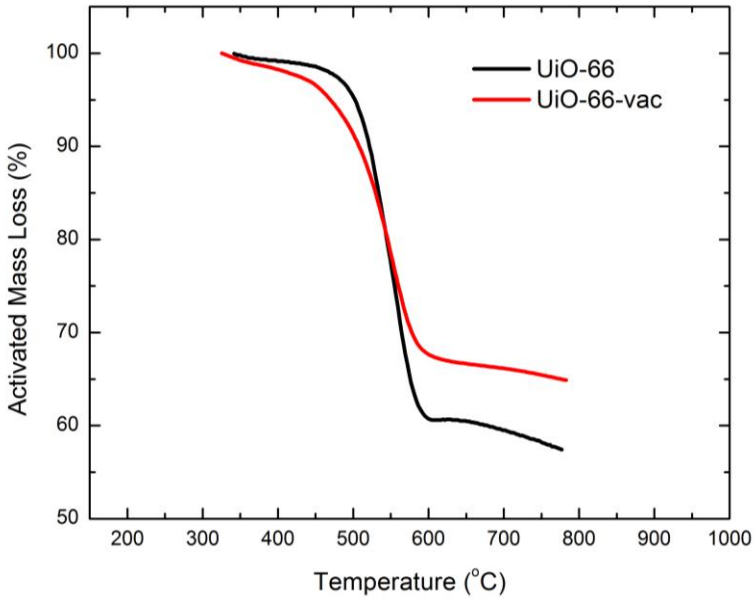

Figure 7. Activated mass loss curves for UiO-66 and UiO-66-vac. TG data for UiO-66 replicated from Tulig et al.[36]

Multiple batches of UiO-66-ox were synthesized with an average surface area of 1158 ± 84 m^2 g^{-1}; significantly lower than the previously published surface area of 1410 m^2 g^{-1}.[33] Disagreement in surface areas may be due to a higher degree of oxalic acid functionalization with missing linker defect sites in UiO-66-vac than in experiments featured in previous literature, which would cause the resulting surface area to decrease. It is also likely consequential of surface area differences in the mixed UiO-66-vac precursor batch used in the syntheses. Regardless, the observed drop in surface area alludes to the expected inclusion of carboxyl groups into the MOF's framework after treatment with oxalic acid.

One batch of UiO-66-ox-Cu was then made through copper insertion on activated UiO-66-ox. The BET surface area was 1116 m^2 g^{-1}, exhibiting negligible surface area loss from the experimentally determined 1158 ± 84 m^2 g^{-1} for UiO-66-ox. One batch of

Cu @ UiO-66 was also synthesized, using parent UiO-66 as the MOF precursor, for comparison to UiO-66-ox-Cu, in order to gauge effects of defects on metal loading sites. Parent UiO-66 had a surface area of 1111 m^2 g^{-1}, in close agreement with experimental values from previous literature.[21,36,42] Figure 8 displays the N_2 physisorption curves used for BET surface area analysis of all materials, where the resulting surface area for Cu @ UiO-66 was calculated as 781 m^2 g^{-1}: a 30% loss from the parent material. Loss in surface area post-impregnation has been observed in similar systems, where a 31% BET surface area loss was observed by Guo et al. following Pt impregnation (10.7 wt%). in UiO-66-NH_2[37] and 67% loss after Pd impregnation in MOF-5 reported by Sabo et al.[43] This also may suggest the nature of Cu incorporation into Cu @ UiO-66 is predominantly representative of an impregnation of the metal into the pore space of the MOF, rather than coordination of copper to binding sites. Surface area loss is less significant in UiO-66 MOFs with open carboxyl functional groups because incoming Cu^{2+} ions are predicted to bind to the carboxylic acid sites instead of becoming trapped in the pore space. The PXRD patterns in Figure 9 for all materials suggest the structural properties of UiO-66 are maintained throughout all of the samples following copper insertion. BET surface areas for all materials are summarized in Table 1.

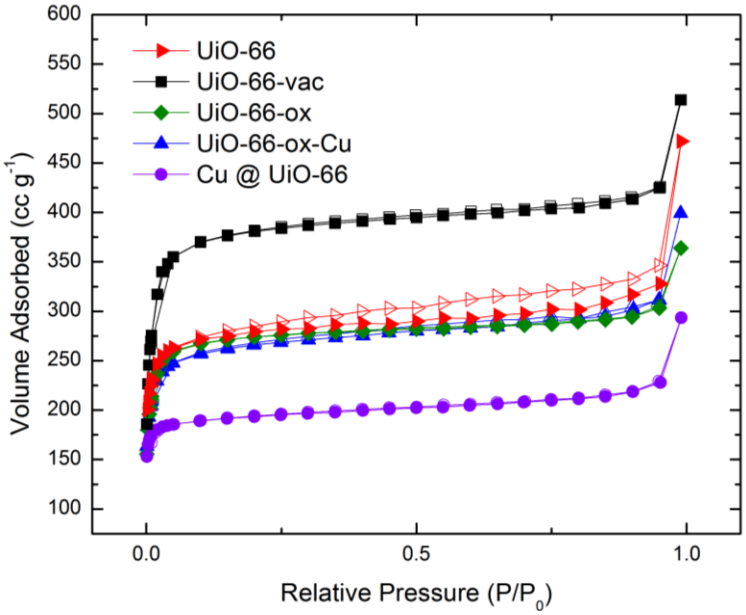

Figure 8. Nitrogen physisorption isotherm curves at 77 K for UiO-66-vac, UiO-66-ox, UiO-66-ox-Cu, and Cu @ UiO-66. Open symbols—desorption, closed symbols—adsorption.

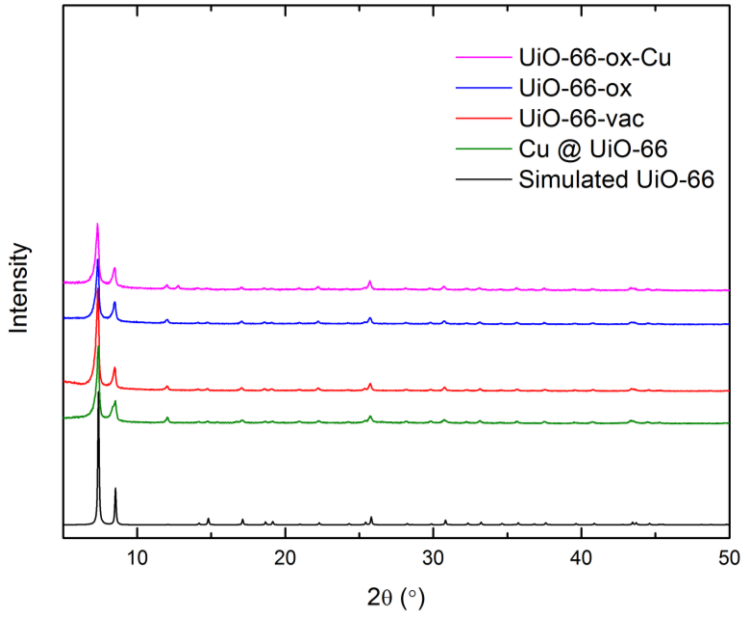

Figure 9. Comparison of PXRD patterns of UiO-66-vac, UiO-66-ox, and UiO-66-ox-Cu to the theoretical diffraction pattern of UiO-66.

Table 1. Surface areas, pore volumes, and copper loadings for activated materials, with previously synthesized UiO-66-COOCu and UiO-66-$(COOCu)_2$.

	Copper Weight Percent (wt %)				
MOF	**Experimental**	**Theoretical[c]**	**Fraction of Theoretical Loading**	**Surface Area (m^2 g^{-1})**	**Total Pore Volume (cc g^{-1})[a]**
UiO-66	----	----	----	1111	0.73
Cu @ UiO-66	4.51	0	----	781	0.46
UiO-66-vac	----	----	----	1534	0.80
UiO-66-ox	----	----	----	1158	0.59
UiO-66-ox-Cu	4.84	5.50	0.88	1116	0.56
UiO-66-COOH[b]	----	----	----	658	0.28
UiO-66-COOCu[b]	7.88	9.62	0.82	564	0.24
UiO-66-$(COOH)_2$[b]	----	----	----	364	0.22
UiO-66-$(COOCu)_2$[b]	3.15	14.52	0.22	357	0.18

[a] Measured at $P/P_0 = 0.5$

[b] Experimental values from Garcia-Gutierrez.[28]

[c] Theoretical loadings based on coordinating one Cu^{2+} ion per two free carboxylic acid groups

3.1.2 Comparison of Structural Properties for Copper Functionalized UiO-66 MOFs

MOF crystals were observed to change from white to light blue, indicative of copper (II) compounds.[44] These physical changes, illustrated in Figure 10, have been observed previously with MOFs containing copper carboxylate functionalities[28] and Cu metal centers[13].

Figure 10. Comparison of UiO-66 before (left) and after (right) copper insertion

Newly synthesized UiO-66-ox-Cu and Cu @ UiO-66 were compared to UiO-66-COOCu and UiO-66-$(COOCu)_2$, whose BET surface areas are also reported in Table 1. UiO-66-ox-Cu exhibits the highest surface area and lowest loss in surface area from its parent precursor among the materials studied. This is due to copper carboxylate functionalities residing away from pore openings near the Zr metal center clusters, mitigating pore blockage. UiO-66-COOCu and UiO-66-$(COOCu)_2$ instead have functional groups on the linkers surrounding the pores of the MOF, which was previously hypothesized to result in partial pore blocking for incoming guest molecules.[28]

Copper loadings on all activated materials were experimentally quantified through ICP-OES, as detailed in Section 2.2.4. Copper weight percents in Table 1 were averaged over multiple readings for the new materials Cu @ UiO-66 and UiO-66-ox-Cu. The copper content results are normalized by taking the ratio of the experimentally determined copper weight percent over the theoretical copper weight percent. Theoretical copper weight percents were calculated by taking the hypothetical number of free

carboxylic acid groups in UiO-66-ox, UiO-66-COOH, and UiO-66-$(COOH)_2$ respectively, per theoretical unit cell. For example, the number of carboxyl binding sites in UiO-66-COOH and UiO-66-$(COOH)_2$ are the number of carboxylic acid groups on each ligand for the respective materials. Similarly, this number for UiO-66-ox was derived from the previous approximation of half of the missing linker sites becoming populated by oxalic acid[33], as mentioned earlier, where the number of oxalic acid species is assumed to be equal to the number of free carboxylic acid sites in the material. The theoretical copper loading for parent UiO-66 was subsequently assumed to be zero, since the ideal unit cell has no open carboxylic acid groups.[21] Furthermore, for finding the theoretical Cu weight percent, it was assumed that one Cu^{2+} ion binds to two carboxyl groups to assure charge neutrality. The fraction of theoretical Cu weight percent in Table 1 was then found by taking the ratio of the experimentally observed copper weight percent from ICP-OES measurements over the calculated theoretical one.

Despite the highest number of theoretical carboxyl binding sites for copper residing in UiO-66-$(COOCu)_2$, this MOF possessed the lowest copper content, whereas UiO-66-COOCu had the highest, which was previously attributed to steric hindrance of Cu ions towards the dicarboxylate ligands in UiO-66-$(COOH)_2$.[28] UiO-66-ox-Cu reaches the highest fractional loading, suggesting most of the theoretical carboxylic acid sites become populated with copper during metal insertion. However, the close to theoretical loading may also be due to copper impregnation, which is likely more prevalent in UiO-66-ox-Cu due to greater pore accessibility that is otherwise hindered by the linker functionalities in UiO-66-COOH and UiO-66-$(COOH)_2$. In any case, this result alludes to a greater accessibility for metal cations to carboxyl binding groups in the defect-

functionalized UiO-66-ox-Cu. Cu @ UiO-66 surprisingly possessed comparable Cu loadings to the MOFs with uncoordinated carboxylic acid binding sites. This is attributed to the copper becoming impregnated in the pore space during the post synthetic modification, as well as some –COOCu coordination from missing linker sites inherent in the parent UiO-66 framework.

MOFs have been shown previously to exhibit decreases in their thermal stability following metal incorporation[37], so TGA was employed to study the impact of copper insertion into the defective UiO-66 system. Figure 11 shows the activated mass loss curves for the four copper functionalized UiO-66 derived MOFs. Higher mass loss percentages are observed for UiO-66-COOCu and UiO-66-$(COOCu)_2$ due to their larger linker molecules, and subsequently larger organic mass fractions than the other two materials. UiO-66-ox-Cu and Cu @ UiO-66 exhibit thermal stabilities close to that of the parent UiO-66 MOF, which features framework degradation above 500 ℃.[45] UiO-66-COOCu and UiO-66-$(COOCu)_2$ were also shown to possess thermal stabilities close to their respective parent MOFs, UiO-66-COOH and UiO-66-$(COOH)_2$, after copper coordination, with loss of structural integrity close to 100 ℃. Negligible stability loss after metal coordination to UiO-66 has also been observed in the grafting of lithium tert-butoxide in a previous study[46], where the insignificant destabilization of the framework from the metal guest species appears similar to the copper carboxylates in this study. It is therefore concluded that post synthetic modification of carboxylic acid groups with copper on UiO-66 does not result in any significant observable loss in thermal stability, but rather this characteristic can be predicted to be the same as the parent MOF precursor.

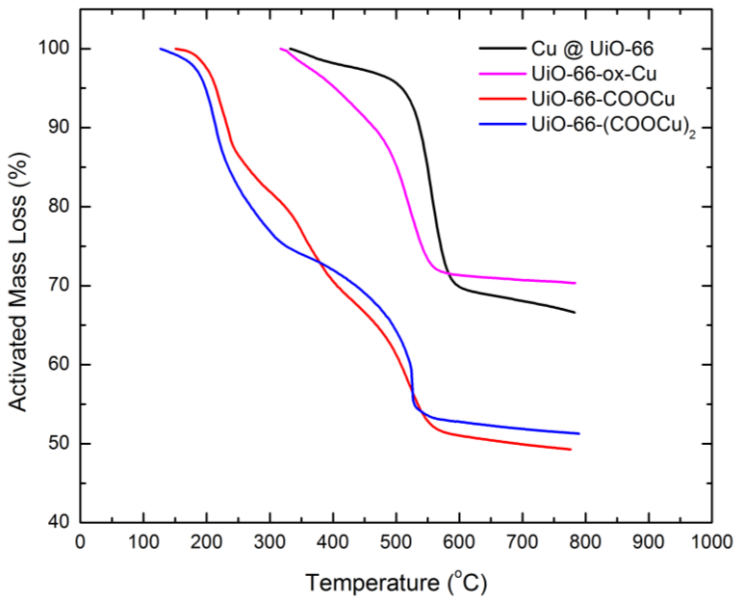

Figure 11. Activated mass loss curves for MOFs following metal insertion. Data for UiO-66-COOCu from Garcia-Gutierrez[28]

3.2 Kinetic Studies on Metal Loading

Metal loading times for UiO-66-$(COOCu)_2$ and UiO-66-ox-Cu were varied to study the kinetics of copper insertion on the MOFs. Loading time was varied in effort to probe possible mass transfer limitations, such as diffusion, of copper into the materials. These two MOFs were chosen due to their contrasting hypothetical coordination sites for copper, as illustrated previously in Figure 5, which may provide insight into mass transfer limitations for metal insertion into varying active –COOH locations. Although previous work studying the effect on metal loading into MOFs by varying loading time have not been performed to the best of our knowledge, a study on UiO-66 and UiO-66-NH_2 on phosphate uptake in aqueous media showed phosphate uptake to increase with loading time in both materials, until an equilibrium maximum loading was reached, as expected.[47]

Analogous uptake behavior in porous iron oxide media for hexavalent chromium ions was also observed by Shi et al.[48], however this material is not microporous like the samples investigated here, so the uptake mechanism would differ significantly.

Copper loading times of 6, 12, and 24 h were used for the time trial experiments, where all other parameters for metal insertion as detailed in Section 2.1.2.5 were kept constant. Labeling nomenclature for the materials is as follows: MOF name-metal insertion time; for example, UiO-66-ox-Cu loaded with copper for 6 hours is named UiO-66-ox-Cu-6h. The same parent MOF batches were used to synthesize 6 and 12 hour batches of UiO-66-ox-Cu and UiO-66-$(COOCu)_2$, respectively, for consistency in textural properties. ICP-OES was used to ascertain metal loadings of the samples, which are shown in Figure 12. Trends in metal loading vary significantly between UiO-66-ox-Cu and UiO-66-$(COOCu)_2$. UiO-66-ox-Cu-6h displays a lower copper loading than observed with the MOF at higher metal insertion times, as expected. Relatively higher loadings at 12h and 24h are observed as reaction time increases. UiO-66-ox-Cu-12h is shown to have a higher copper content than UiO-66-ox-Cu-24h, and also exceeds the theoretical maximum loading of the material. This result is puzzling, but may be due to UiO-66-ox-Cu-12h and UiO-66-ox-Cu-24h being made from different batches of UiO-66-ox, as the location and number of carboxyl binding functionalities are not controlled between batches of the parent MOF, which could impact metal transport to active sites in each framework. It may also indicate the material is approaching a maximum loading, and metal loading experiments at longer times are necessary to confirm this. Overshooting the theoretical maximum loading of UiO-66-ox-Cu suggests a significant amount of the detected copper exists as impregnated metal, instead of as copper

carboxylate functionalities. The uncontrolled defects and subsequent carboxylic acid functionalities involved in the synthesis of UiO-66-ox may also cause there to be more available carboxylic acid binding sites for guest copper species to bind to during the reaction than expected. No direct correlation can be ascertained between copper loading and time for UiO-66-ox-Cu.

Lower copper loadings were observed at all loading times for UiO-66-$(COOCu)_2$, suggesting more significant binding limitations for metal loading exists in this system. The mass fraction of copper in UiO-66-$(COOCu)_2$ counterintuitively decreased with increasing metal loading time. The fractional loading at 6h suggests there is initially a high uptake of copper into the material. This large initial uptake is likely consequent of the relatively high theoretical loading from two free carboxyl binding sites per organic linker, as reflected by the MOF's high theoretical loading relative to the other materials in this study of 14.52 wt% copper. As time increases from 12h to 24h, the degree of copper loss decreases, suggesting the loading may be approaching equilibrium, although testing with longer loading times would be required to confirm this. Lower average copper content for UiO-66-$(COOCu)_2$ at all loading times may be due to steric hindrance between the copper carboxylate functionalities amongst one another as more copper coordinates to the binding sites on the terepthalate linkers. The close hypothetical proximity of the copper carboxylate functionalities to one another may destabilize the Cu-COO^- bonds, making copper binding and retention unfavorable. The loss of copper over time for UiO-66-$(COOCu)_2$ and between 12h and 24h for UiO-66-ox-Cu is puzzling, but it may be subsequent of solvent effects in the copper loading reaction. The solvent used (DMF) is slightly alkaline, but pH measurements show the reaction solution

becomes acidic after the addition of $Cu(NO_3)_2$, likely due to the formation of nitric acid from the deprotonation of carboxylic acid groups on the MOFs by the introduced nitrate anions, as well as water impurity in DMF. Subsequently, the reagent solution could be equilibrating as reaction time increases, where the functionalized copper on –COOCu groups may become displaced as carboxyl groups are reprotonated by acidic species. This behavior is more pronounced in UiO-66-$(COOCu)_2$, possibly due to the aforementioned instability of –COOCu groups relative to UiO-66-ox-Cu, and a greater accessibility of copper carboxylate groups on ligand functionalities, which would facilitate metal leaching through these solvent effects. However, this mechanism may also explain why there is a loading decrease from 12h to 24h loadings on UiO-66-ox-Cu. Longer metal insertion times and pH measurements over the reaction time period are required to further probe this hypothesis. Furthermore, it is suggested that using a copper salt that produces a basic anion in solution, such as copper acetate, could be used to contrast the effects of acidity on metal leaching during the copper loading process.

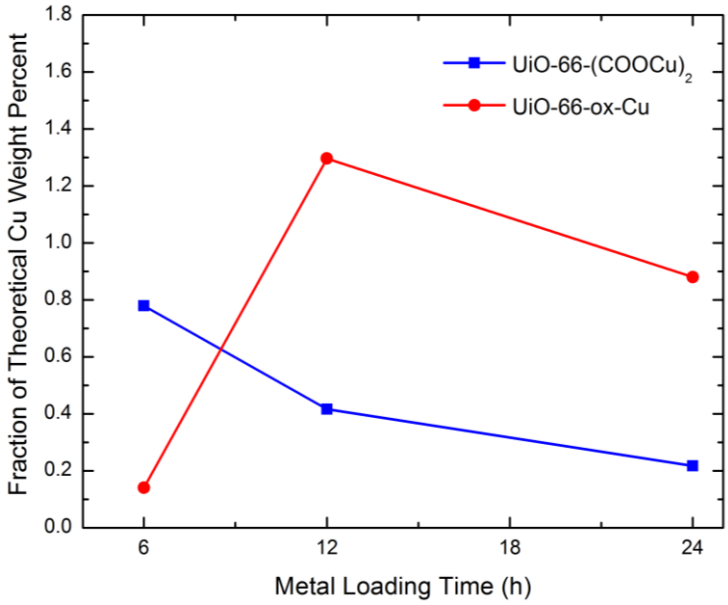

Figure 12. Change in copper content for UiO-66-ox-Cu and UiO-66-$(COOCu)_2$ for varying metal loading times. Loading for UiO-66-$(COOCu)_2$ at 24h taken from Garcia-Gutierrez.[28]

3.3 Isothermal Water Vapor Adsorption Measurements

Although adsorption affinity is dependent on a multitude of factors, adsorbent hydrophillicity is generally detrimental for the adsorption of other species in humid streams, since it leads to competitive adsorption in the binding sites of the materials between the adsorbate of interest and water.[15,49] However, a recent screening of hydrophobic MOFs by the Moghadam et al. showed that high hydrophobicity in MOFs also lowered TIC adsorption affinity, and the most favorable MOFs for ammonia selectivity exhibited moderate hydrophobicity.[50] UiO-66 is slightly hydrophobic[49], and adding missing linker defects increases water binding affinity.[31] So, water vapor adsorption measurements were taken for UiO-66-vac, UiO-66-ox, and UiO-66-ox-Cu

MOFs to gauge hydrophobicity of the materials following defect incorporation and subsequent copper coordination.

Water adsorption isotherms at 25 ℃ for the aforementioned MOFs are shown in Figure 13, along with a previously obtained isotherm for parent UiO-66.[51] Water capacities are normalized by mass of adsorbent for the curves. All materials exhibit lower pressure hysteresis (H1), which is common for microporous materials.[52] Pore filling appears to occur at the same step (20% RH) for UiO-66 and UiO-66-vac, suggesting the pore sizes are close to one another, despite missing linker moieties in UiO-66-vac.[20] Water adsorption simulations on UiO-66 have predicted the same increase in water adsorption after the introduction of missing linker defects observed here between UiO-66-vac and the parent material.[31] Interestingly, UiO-66-ox and UiO-66-ox-Cu exhibit more hydrophobic behavior, despite the introduction of hydrophilic carboxyl and unsaturated copper functionalities, respectively. Increased water vapor loadings from UiO-66-ox to UiO-66-ox-Cu are due to the inclusion of metal cations, which have high affinities towards water, despite increased adsorbent density following metal loading.[20] Water retention amounts following desorption for all samples are within error of one another. N_2 physisorption experiments show significant surface area losses for UiO-66-ox and UiO-66-ox-Cu only; this information is provided in Table 2, along with the water loadings for each MOF at 90% RH. UiO-66-vac shows no observable change in surface area, confirming the retention of water stability of the material with missing linker defects. PXRD patterns in Figure 14 confirm structure retention after H_2O exposure, although the high degree of surface area loss in UiO-66-ox-Cu may still indicate degradation that does not affect the long-range order of the crystalline material, which

would be captured by diffraction measurements. One previously proposed mechanism for MOF degradation after water exposure involves metal-ligand bond replacement with water molecules, which was said to be more favorable in systems where the metal centers are less coordinated[53]. The existence of missing linker defects in UiO-66-ox-Cu in contrast with parent UiO-66 aligns with this proposed mechanism, and the added steric interference from coupled –COOCu groups near the zirconium metal centers may lead to the proposed metal-ligand replacement mechanism in the presence of water vapor. Strong retention of water from hydrophilic functionalities in UiO-66-ox and UiO-66-ox-Cu during activation of the materials may have caused lower surface area measurements following water vapor adsorption measurements.

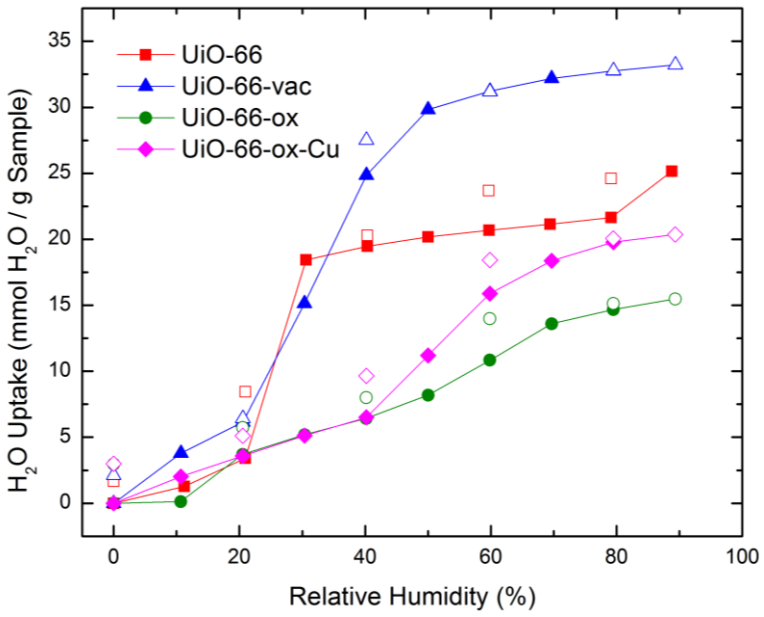

Figure 13. Water adsorption isotherms at 1 bar, 25 ℃, for UiO-66, UiO-66-vac, UiO-66-ox, and UiO-66-ox-Cu. Open symbols – desorption, closed symbols – adsorption. Data for UiO-66 from Shoenecker et al.[51]

Table 2. Water vapor adsorption data and surface area changes in UiO-66-vac, UiO-66-ox, and UiO-66-ox-Cu before and after water vapor adsorption experiments

MOF	Loading at 90% RH (mL g^{-1})	Water Retention at 0% RH (mL g^{-1})	BET Surface Area (m^2 g^{-1})		
			Before	After	Percent Loss (%)
UiO-66-vac	0.59	0.04	1534	1566	-
UiO-66-ox	0.28	0.05	1158	835	28
UiO-66-ox-Cu	0.37	0.05	1116	538	50

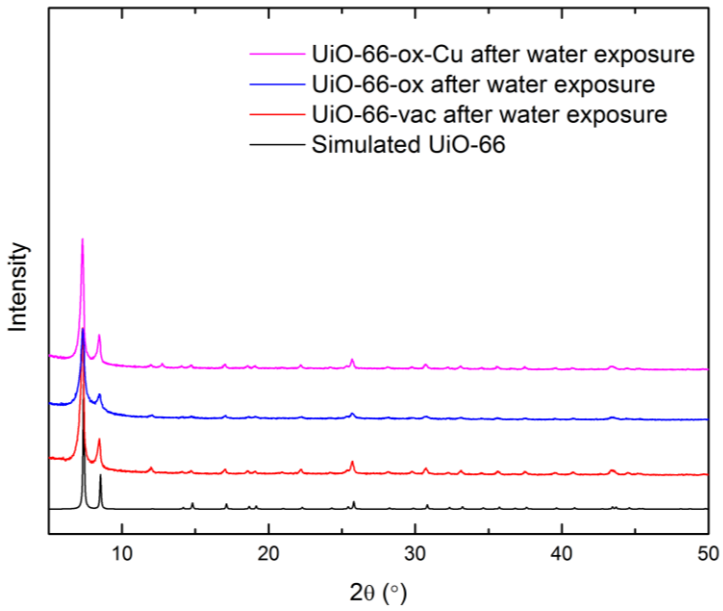

Figure 14. PXRD patterns of UiO-66-vac, UiO-66-ox, and UiO-66-ox-Cu after water vapor adsorption experiments with the theoretical diffraction pattern of UiO-66

Uptake behavior of UiO-66-ox is similar to that of UiO-66-COOH and UiO-66-$(COOH)_2$, which also contain carboxylic acid functionalities, as evidence by Figure 15. The isotherm trends for all three MOFs indicate weak affinity for water. Polar carboxylic acid groups on UiO-66-$(COOH)_2$ have been previously observed to create Type I water isotherms[54], which are indicative of microporous materials with favorable adsorbate-

adsorbent interactions[52,55], in contrast to the more sigmoidal shapes observed here, and further reproducibility on these measurements should be carried out to check for consistency. Because all three MOFs are of the same isostructural family and feature carboxylic acid functional groups, water uptakes for the MOFs primarily differ depending on surface area and pore accessibility, where UiO-66-ox has the highest surface area and observed water uptake. The high degree of hysteresis in UiO-66-ox as compared to the other two MOFs suggests irreversible loading between water molecules and the carboxylic acid functional groups in the MOF[49], and therefore, a higher degree of the carboxyl functionalities in UiO-66-ox are likely accessible at for binding and retention of water than in the other two MOFs.

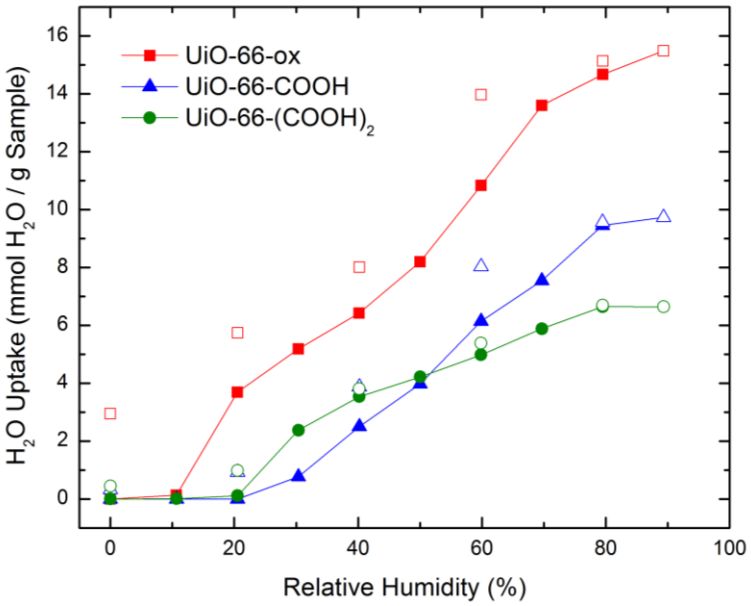

Figure 15. Water adsorption isotherms at 1 bar, 25 ℃ for UiO-66-ox, UiO-66-COOH, and UiO-66-$(COOH)_2$. Open symbols – desorption, closed symbols – adsorption.

The water isotherm for UiO-66-ox-Cu is contrasted with the previously tested UiO-66-COOCu and UiO-66-$(COOCu)_2$ in Figure 16. Type I isotherms were observed for UiO-66-COOCu and UiO-66-$(COOCu)_2$, indicating favorable water adsorption.[28]

Close uniformity in isotherm shape and water loadings exist at each humidity point for UiO-66-COOCu and UiO-66-$(COOCu)_2$, which is not evident for their parent MOFs in Figure 15, implying hydrophilic metal sites are coordinated similarly in these two materials. Water uptake in UiO-66-ox-Cu deviated from this behavior, where the isotherm only starts to display significant water uptake at 40% RH, despite exhibiting the highest water capacity at 90% RH of all samples. The sigmoidal shape of the adsorption curve for UiO-66-ox-Cu is likely consequent of the partial degradation of the material, as explained earlier for Figure 13. Vapor loadings do not correlate with Cu mass fractions for the MOFs, made apparent by comparison with the data listed previously in Table 1. Greater hydrophobicity for UiO-66-ox-Cu suggests copper is mostly present in locations less accessible to water vapor at lower pressures than with UiO-66-COOCu and UiO-66-$(COOCu)_2$. Because carboxyl functionalities for binding copper are believed to be located inside the framework of UiO-66-ox, it is possible the copper in UiO-66-ox-Cu is largely coordinated within the pore space, whereas copper carboxylate sites on UiO-66-COOCu and UiO-66-$(COOCu)_2$ may be mostly located externally on the MOF crystals, leading to the Type I behavior from the easily accessible copper binding sites for H_2O. Higher water retention at 90% RH in UiO-66-ox-Cu may be due to a higher accessibility of copper groups in the material following the partial degradation of the structure, although any rearrangement of functional groups in the sorbent are difficult to confirm here.

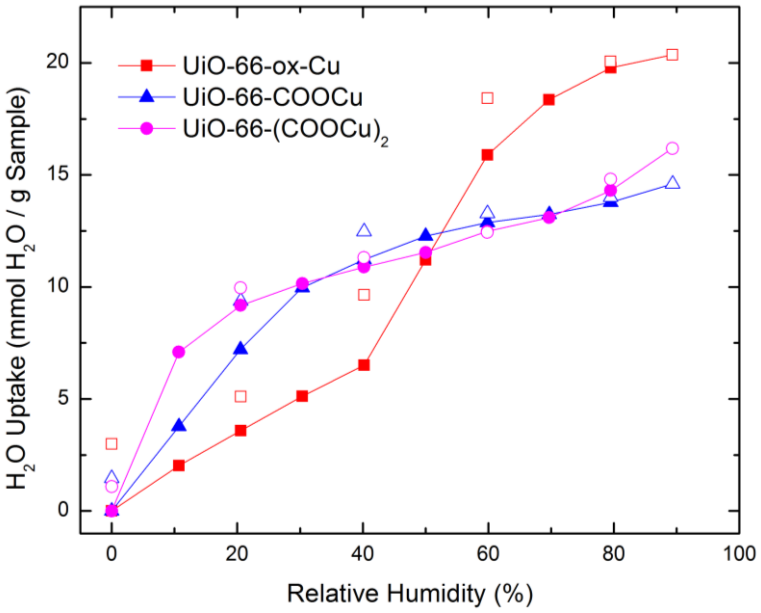

Figure 16. Water adsorption isotherms for copper-inserted MOFs: UiO-66-ox-Cu, UiO-66-COOCu, and UiO-66-$(COOCu)_2$. Open symbols – desorption, closed symbols – adsorption.

3.4 Ammonia Breakthrough Measurements

3.4.1 Dynamic Ammonia Breakthrough Capacities for New Materials

Breakthrough measurements are the preferred method of evaluating the performance of materials used for air purification, as it provides insight into any mass transfer limitations that may exist for the material and the challenge gas, and allows for the simulation of conditions that exist in the end application (i.e. humidity, concentration, etc.), which is not the case for equilibrium measurements.[15,56] Both dry and humid (80% relative humidity) ammonia breakthrough experiments were run for Cu @ UiO-66, as well as UiO-66-$(COOCu)_2$ and UiO-66-ox-Cu samples synthesized at 6, 12, and 24 hour copper loadings. Dynamic ammonia capacities were calculated using Equation 1, where

the breakthrough time (t_b) was defined as the time required for detection of 50 ppm NH_3 to align with the OSHA Permissible Exposure Limit (PEL) for ammonia.[5]

$$C = \frac{\dot{n}_{NH_3} t_b}{m_a} \quad (1)$$

Color changes were observed in both dry and humid ammonia breakthrough runs for all MOFs subjected to post synthetic modification with copper in this study. This physical change is attributed to NH_3 binding with both coordinated and impregnated Cu (II), as uncoordinated copper can form polynuclear complexes[57] capable of binding adsorbates such as ammonia, which has also been reported with coordinatively unsaturated metal sites in MOFs.[55] Observable evidence of ammonia-copper interactions is noted in Figure 17, where a color change of the sample from light to dark blue is seen. This is indicative of ammonia-copper interactions in MOFs, as described previously with HKUST-1.[17] This color change was also observed to be irreversible under activation conditions for the respective MOFs. Ammonia enters the bed from the top, and creates the top-to-bottom variation in color change as the experiment time progresses.

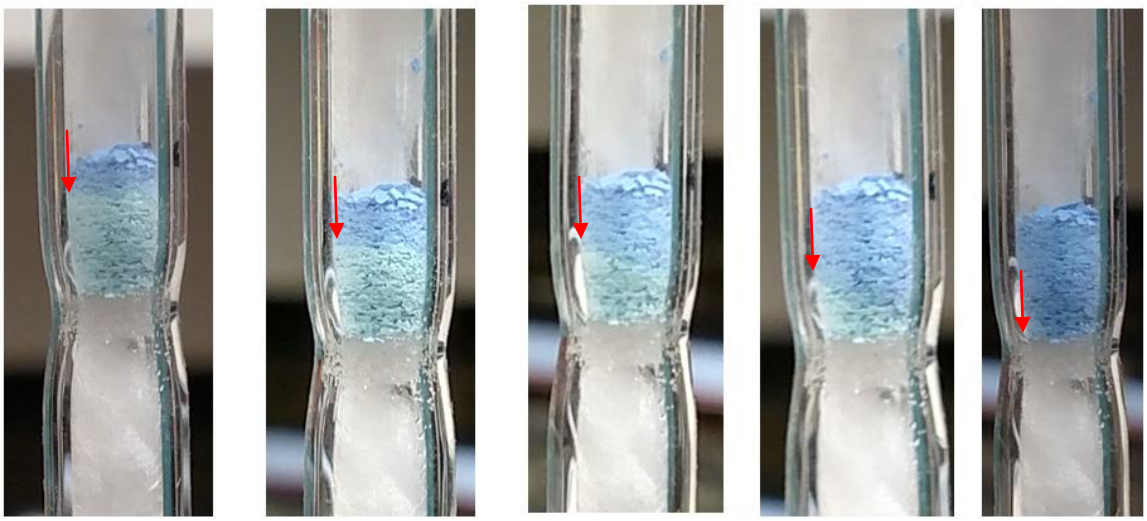

Figure 17. Progressive color change of UiO-66-$(COOCu)_2$ during ammonia breakthrough experiment. Dark blue areas indicate regions exposed to ammonia, and light blue sections are unexposed MOF. Time lapse of NH_3 exposure progresses left to right.

Dry and humid dynamic breakthrough curves were collected for Cu @ UiO-66. Previously reported experimental ammonia capacities for UiO-66 are provided for comparison with Cu @ UiO-66.[42] Dynamic uptake capacities are provided in Table 3. Increased uptake capacity for Cu @ UiO-66 in dry conditions is attributed to copper carboxylate sites forming on inherent missing linker sites[58] in parent UiO-66, though it is important to note the coordination nature of copper in the MOF is unknown. Increases in uptake are not as significant as ones observed for UiO-66-COOH and UiO-66-$(COOH)_2$[28] however, and this is attributed to the small number of average missing linker sites (1 out of 12)[22] available to create coordinatively unsaturated copper sites that can strongly bind ammonia. Capacity drop in humid conditions is likely related to non-primary chemical bonding between adsorbates in the mixed stream. Synergistic binding effects have been observed for mixed water and ammonia streams[59], but these are consequent of cooperative hydrogen bonding between the adsorbate species and secondary binding on

chemisorptions sites.[18] DFT calculations by Watanabe et al.[60] suggest secondary binding of NH_3 and H_2O on Cu sites in HKUST-1 is less favorable, based on their pair interaction energies, than observed with individual molecules, and a similar phenomena is hypothesized in this study for coordinated copper in UiO-66 type MOFs. Greater relative abundance of these weaker interactions in wet breakthrough experiments are shown by the desorption curves for Cu @ UiO-66 in dry and humid streams in Figure 18 and Figure 19, respectively. The more shallow desorption curve in Figure 19 is consequent of mass transfer limitations during the wet breakthrough experiment, caused by weakly adsorbed species leaving the adsorbent.[59] Cooperative physisorption effects are likely constrained in Cu @ UiO-66, due to pore space blocking by the impregnated metal, evidenced by the lower pore volume reported earlier in Table 1. This is thought to create a more competitive bonding environment between water and ammonia on the active metal sites, which has previously been attributed to a decrease in material acidity from water bonding[59], creating a less favorable adsorption environment for basic ammonia molecules.

Table 3. Dynamic breakthrough capacities of ammonia for UiO-66, Cu @ UiO-66, UiO-66-ox, and UiO-66-ox-Cu under dry and humid conditions.

MOF	**NH_3 Dynamic Capacity ($mmol\ g^{-1}$)**	
	Dry (0% RH)	**Wet (80% RH)**
UiO-66[a]	1.79	2.75
Cu @ UiO-66	2.25	1.15
UiO-66-ox	2.50[b]	2.30
UiO-66-ox-Cu	4.31	4.02

[a] Data reported from Jasuja et al.[42]

[b] Data reported from DeCoste et al.[33]

Dry and humid dynamic breakthrough capacities for UiO-66-ox and UiO-66-ox-Cu were also contrasted, and are included in Table 3. In contrast to the differences in ammonia adsorption between UiO-66 and Cu @ UiO-66, large increases in dynamic ammonia capacities were observed before and after metal insertion for UiO-66-ox, where UiO-66-ox-Cu exhibited a 75 % increase in humid capacity and 72 % increase under dry conditions. Ammonia breakthrough curves in Figure 18 and Figure 19 further delineate greater favorability of ammonia adsorption in UiO-66-ox-Cu over Cu @ UiO-66. The difference in ammonia capacity changes before and after metal insertion between the two MOF systems is due to the role of defects in copper coordination. Greater pore volume and surface area measurements, for UiO-66-ox-Cu imply adsorption sites within the framework are more accessible to guest species. Physisorption of ammonia subsequently appears more prevalent in the UiO-66-ox-Cu system than with Cu @ UiO-66, as

adsorbent-adsorbate interactions are promoted, as evidenced by more shallow desorption curves for UiO-66-ox-Cu than Cu @ UiO-66 in Figure 18 and Figure 19.

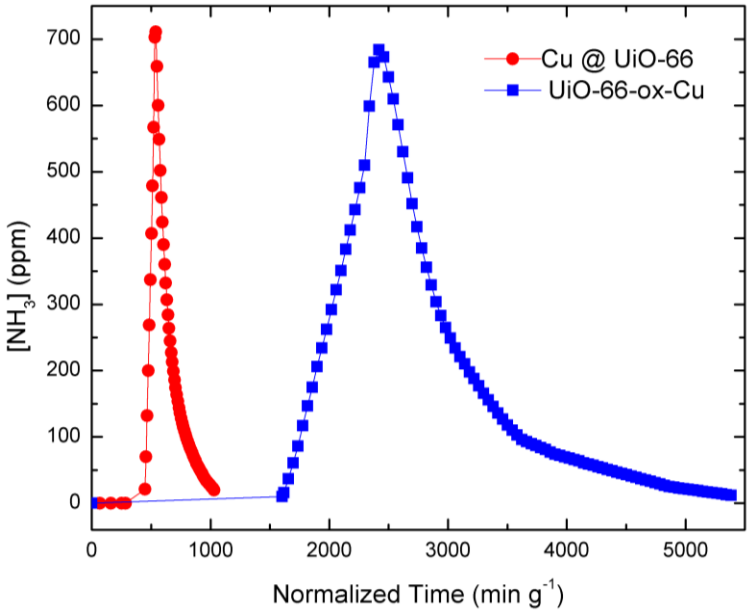

Figure 18. Dry ammonia breakthrough curves for Cu @ UiO-66 and UiO-66-ox-Cu

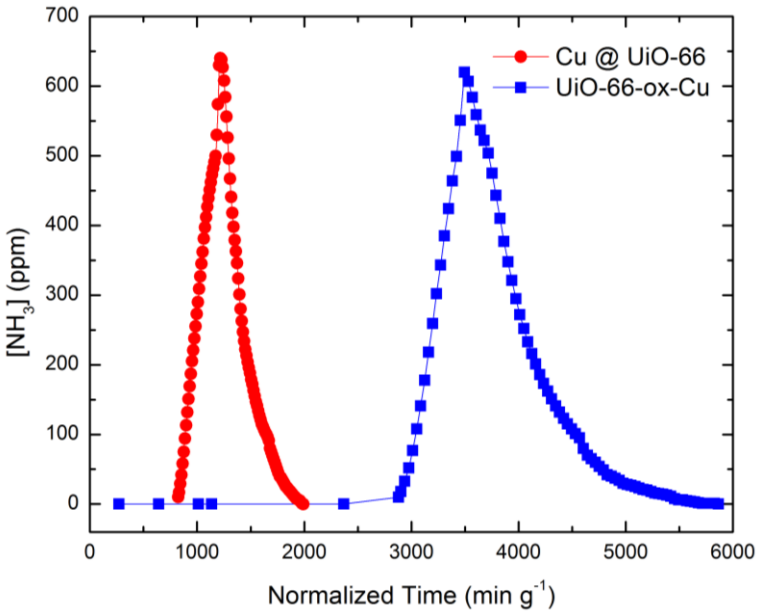

Figure 19. Humid ammonia breakthrough curves for Cu @ UiO-66 and UiO-66-ox-Cu

Comparing dynamic uptakes of the MOFs in this study with the metal loadings reported in Table 1 suggests the respective coordination environments and accessibilities of copper sites in the MOF structures are more impactful for ammonia uptake than copper loading. Importance of functional group orientation and accessibility for NH_3 adsorption has been shown previously through Monte Carlo simulations on IRMOF-1 and MIL-47, where steric effects for –OH groups positions on MIL-47 resulted in a lower ammonia loadings, despite having a larger pore size than IRMOF-1.[61] No direct correlation is observed between metal loading and ammonia uptake performance for the UiO-66 type MOFs post-copper functionalization. In fact, Figure 20 shows UiO-66-$(COOCu)_2$, which was found to have the lowest copper content, is the highest performing MOF for ammonia uptake under wet and dry conditions. This is likely due to the accessibility of copper binding sites for ammonia on functional groups located directly in pore openings.[28] In contrast, the copper loading for Cu @ UiO-66 is in the middle of the investigated MOFs, but exhibits the lowest NH_3 dynamic capacities under wet and dry conditions. It is hypothesized that the lack of –COOH coordination sites for copper prevented the formation of –COOCu groups in the framework for ammonia binding. Furthermore, the accessibility of copper impregnated in the UiO-66 framework is much lower than the other MOFs, particularly the similar UiO-66-ox-Cu system, resulting in lower uptakes.

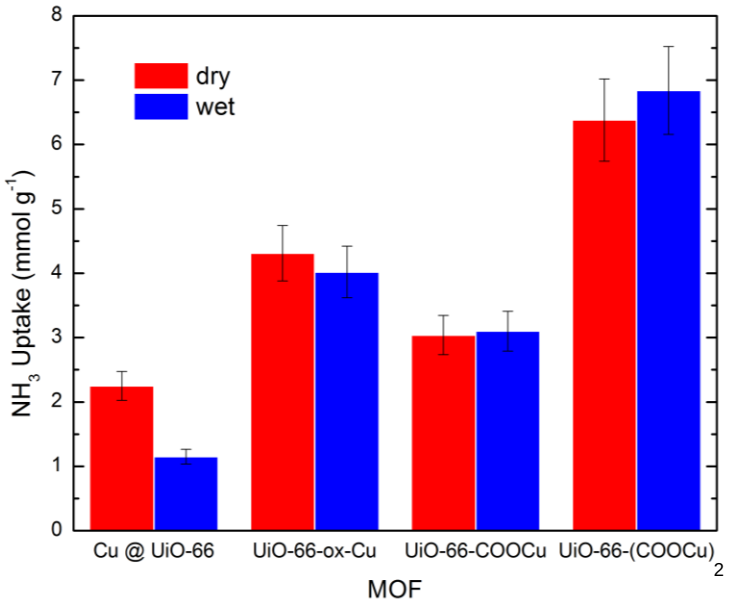

Figure 20. Comparison of dry and wet ammonia breakthrough capacities for UiO-66 type MOFs after post synthetic modification with copper. Data for UiO-66-COOCu and UiO-66-$(COOCu)_2$ taken from Garcia-Gutierrez[28]

MOFs were reactivated following ammonia breakthrough experiments, and BET surface area measurements were taken to study the regeneration of Cu @ UiO-66 and UiO-66-ox-Cu after dry and wet ammonia breakthrough experiments. Table 4 summarizes the change in BET surface area after dry and wet NH_3 exposure for the two MOFs. Cu @ UiO-66 showed no change in surface area after dry ammonia, while the surface area of UiO-66-ox-Cu was almost halved. This may indicate irreversibly adsorbed ammonia molecules in the pore space were hindering N_2 accessibility during the physisorption experiment. The accessible surface area of Cu @ UiO-66 dropped 38% after humid NH_3 exposure, likely due to retained water and ammonia molecules in the crystal lattice. UiO-66-ox-Cu however lost 71 % of its original BET surface area following wet ammonia breakthrough measurements. Furthermore, unlike Cu @ UiO-66, the crystal structure of UiO-66-ox-Cu is not retained after humid ammonia experiments,

as evidenced by the X-ray diffraction patterns shown in Figure 21. The PXRD and N_2 physisorption data suggests ammonia and water synergistically contribute to the degradation of UiO-66-ox-Cu, as large surface area losses were observed for the material under water exposure listed previously in Table 2, and dry ammonia exposure as reported in Table 3, but Figure 21 reveals loss of crystal structure only after wet ammonia breakthrough experiments. It should be noted that the PXRD patterns following water adsorption experiments given previously in Figure 14 showed no structural degradation for the material. Interestingly, PXRD data for UiO-66-ox, provided in Figure 22, does not show the same structural loss as UiO-66-ox-Cu, and this was similarly not observed for Cu @ UiO-66 in Figure 21 or other UiO-66 type MOFs subjected to copper insertion.[28] So, the presence of defects and copper in UiO-66-ox-Cu both affect the degradation of UiO-66-ox-Cu after humid ammonia exposure. One hypothesis is that the coordinated copper in the framework may be in close enough proximity to zirconium metal clusters in the framework to destabilize the bonds between the metal centers and organic linkers, such that water and ammonia guest molecules coordinating to copper sites create sufficient steric interference to degrade the framework around the metal nodes. In the future, copper should also be incorporated into UiO-66-vac to gauge any chemical stability change and ascertain if copper is interacting directly with open zirconium sites in the defective framework to destabilize the structure, or with oxalic acid linkers in UiO-66-ox.

Table 4. BET surface area measurements for Cu @ UiO-66 and UiO-66-ox-Cu after dry and wet NH_3 breakthrough experiments

MOF	Post Dry NH_3		Post Wet NH_3	
	Surface Area (m^2 g^{-1})	Loss in Surface Area (%)	Surface Area (m^2 g^{-1})	Loss in Surface Area (%)
Cu @ UiO-66	794	-	484	38
UiO-66-ox-Cu	614	45	322	71

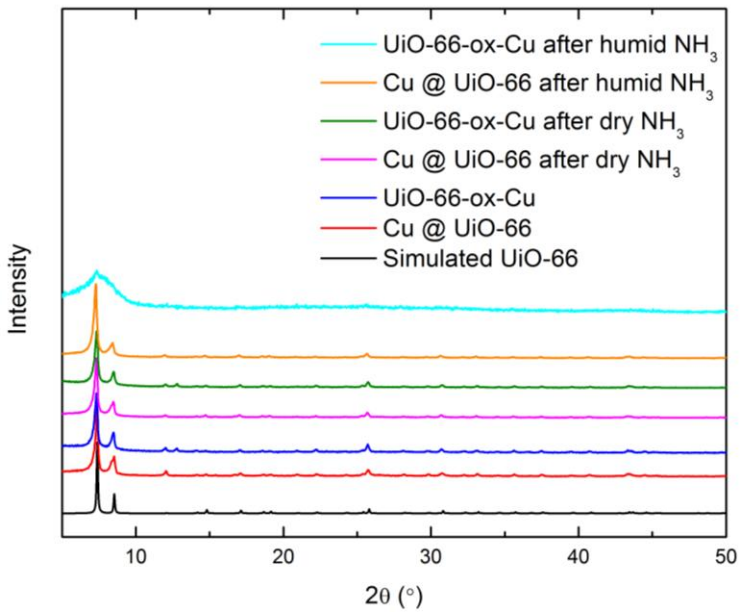

Figure 21. PXRD spectra of Cu @ UiO-66 and UiO-66-ox-cu before and after dry and wet ammonia breakthrough experiments

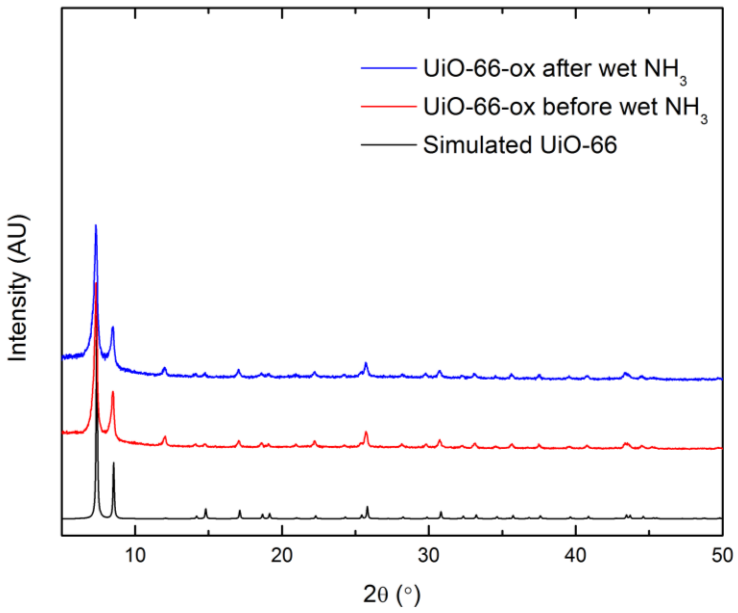

Figure 22. PXRD spectra of UiO-66-ox before and after humid NH_3 exposure

3.4.2 Effect of Copper Loading on Ammonia Breakthrough Capacity

Breakthrough capacities for UiO-66-$(COOCu)_2$ and UiO-66-ox-Cu with varied respective Cu masses, as detailed previously in Section 3.2, were also found to elucidate any trend between metal insertion and ammonia capacity. Figure 23 and Figure 24 show copper content for UiO-66-$(COOCu)_2$ and UiO-66-ox-Cu, respectively, plotted against experimental dynamic ammonia breakthrough capacity under dry and humid conditions. Curves for both dry and wet ammonia streams in UiO-66-$(COOCu)_2$ in Figure 23 exhibit decreases in ammonia capacity with increasing copper content. From about 40% of the theoretical copper loading, no significant change in uptake is observed, suggesting the added copper is not accessible for ammonia coordination. This could be consequent of the copper becoming impregnated inside the MOF instead of coordinated onto ligand carboxyl sites. It may also be due to steric effects between nearby copper carboxylate

groups, hindering the formation of ammonia-copper bonds. Capacities under wet conditions are higher than those observed in dry breakthrough runs, suggesting significant cooperative bonding exists between water and ammonia for this material. Another possible mechanism proposes an enhanced solubility of adsorbates due to micropore filling of water in humid streams. This has been observed for increased CO_2 adsorption on MOFs in humid streams[62], and is a plausible explanation for increased ammonia adsorption in wet streams.

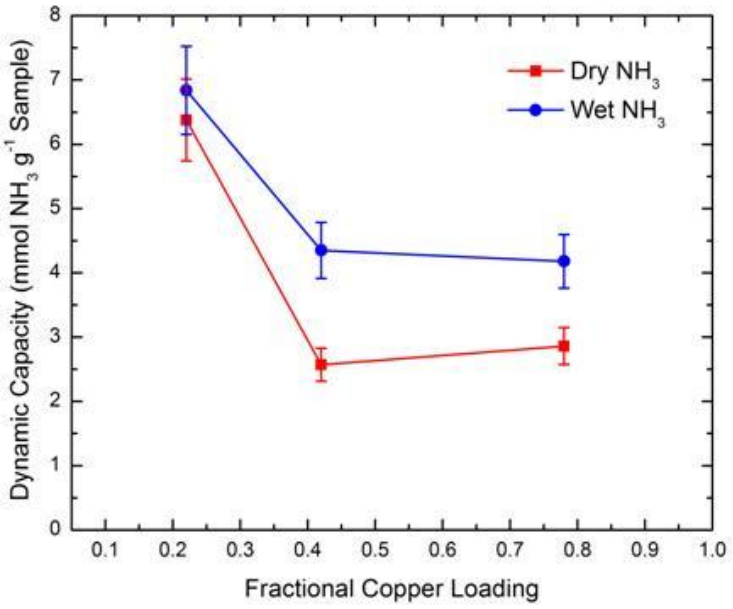

Figure 23. Copper loading UiO-66-$(COOCu)_2$ versus ammonia breakthrough capacity. Wet runs conducted at 80% RH. Capacities at fractional weight percent = 0.22 from Garcia-Gutierrez.[28]

Ammonia uptake behavior for UiO-66-ox-Cu at increasing copper loadings in Figure 24 differs markedly from what was observed for UiO-66-$(COOCu)_2$ Under humid conditions, there is no conclusive change in dynamic capacity with varied Cu mass fractions. Steric hindrance from a higher fraction of copper species in the pore space is hypothesized to prevent the cooperative binding effects between water and ammonia,

similarly to what was seen for higher loadings in UiO-66-$(COOCu)_2$. In particular, the highest copper loading measured for UiO-66-ox-Cu exceeded the theoretical maximum, as previously explained in Section 3.2, so it is likely that a significant amount of copper is impregnated in the pore space, which would exacerbate steric hindrance of ammonia and water guest species. Differences in the location of copper carboxylate functionalities between UiO-66-ox-Cu and UiO-66-$(COOCu)_2$ may suggest that adding these functional groups to linker sites, as in UiO-66-$(COOCu)_2$, creates more accessible binding environment for secondary binding of ammonia and water, which is illustrated in Figure 25.[18] Although the visual pertains to the MOF HKUST-1, the cooperative interactions between ammonia and water following primary binding of ammonia to copper, which is more energetically favorable than water-copper bonding[27], are believed to exist in the UiO-66 system as well. Dry ammonia breakthrough experiments show a gradual increase in uptake capacity, where the highest loading possesses a capacity of 5.10 mmol NH_3 g^{-1} adsorbent. The increasing trend in ammonia uptake suggests maximizing copper loading increases dry ammonia capacity, and breakthrough experiments at higher copper loadings should be conducted to ascertain the maximum possible dynamic breakthrough capacity of the material.

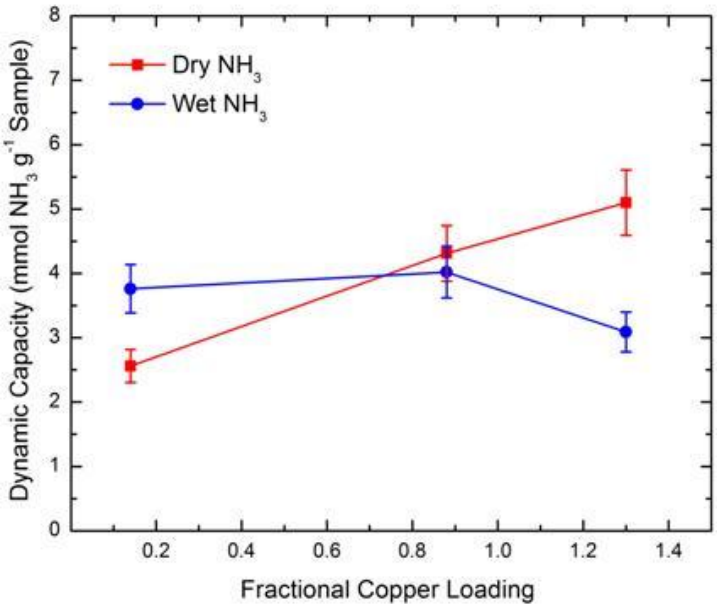

Figure 24. Copper loading in UiO-66-ox-Cu versus ammonia breakthrough capacity. Wet runs conducted at 80% RH.

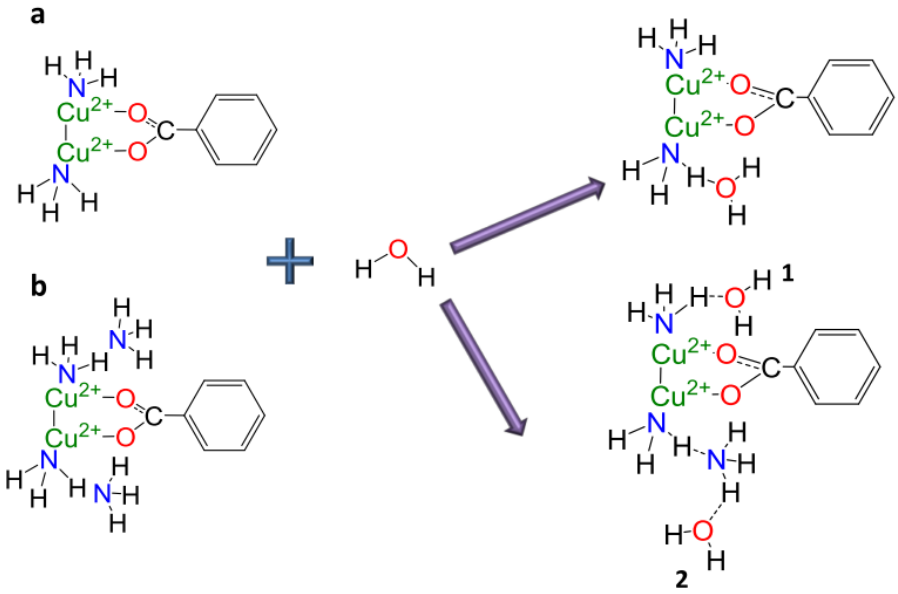

Figure 25. Secondary, cooperative binding schemes of water and ammonia on active sites in HKUST-1. Reproduced from Nijem et al.[18]

CHAPTER 4

CONCLUSIONS AND RECOMMENDATIONS

4.1 Conclusions

A post-synthetic modification procedure on a missing linker version of UiO-66 was used to enhance ammonia capture capabilities of the material via coordination of copper (II) to carboxyl functionalities. UiO-66-vac and UiO-66-ox were synthesized, based on previous literature, as precursor MOFs with carboxylic acid functionalities located within missing linker defect sites. A new MOF, UiO-66-ox-Cu, was created by incorporating copper to the carboxylic acid groups inside UiO-66-ox through a second post synthetic modification step to theoretically yield –COOCu functionalities, which have been shown experimentally and computationally to improve adsorbent affinity for ammonia.[27,28] Water vapor adsorption experiments showed UiO-66-ox-Cu retains structural integrity and hydrophobicity after metal insertion, unlike copper carboxylate MOFs UiO-66-COOCu and UiO-66-$(COOCu)_2$[28], suggesting enhanced ammonia selectivity in humid streams.[50] Large surface area loss in the material suggests there may be partial degradation of UiO-66-ox-Cu in humid streams, however the project scope of designing one-use CBRN filters means the material could still be a feasible sorbent.

Ammonia uptake performances under dry and humid conditions were attained for UiO-66-ox-Cu and Cu @ UiO-66. UiO-66-ox-Cu possessed improved ammonia uptake performance from its parent MOF precursors under dry and humid conditions, whereas Cu @ UiO-66 exhibited minimal increase in dry conditions, and a loss in ammonia uptake capacity under humid conditions. This was attributed to the greater presence of –

COOCu groups in UiO-66-ox-Cu, which possess a high binding energy with ammonia[27], and a greater accessible surface area than Cu @ UiO-66, as suggested by N_2 physisorption experiments at 77 K. Instability of UiO-66-ox-Cu following humid ammonia exposure is observed by BET surface area analysis and PXRD measurements, which is attributed to clustering of water and ammonia at intraframework copper binding sites, destabilizing zirconium-terephthalate bonds due to their close hypothesized proximity to functionalized –COOCu groups. These observations suggest the presence of bulky copper carboxylate groups near the MOF metal center through functionalization on missing linker defect sites lends to the degradation of the material. Furthermore, structural loss only occurs in mixed water and ammonia exposure, indicating cooperative interactions between the adsorbates leading to the degradation of the material.

Kinetic effects of copper loading were studied by varying loading times on MOFs with linker and defect carboxylic acid binding functionalities in UiO-66-$(COOCu)_2$ and UiO-66-ox-Cu, respectively. Decreases in metal loading with increased loading time for UiO-66-$(COOCu)_2$ were attributed to metal leaching via increased solvent acidity, coupled with bond destabilization at higher loadings due to steric hindrance. No direct correlation for metal loading with time could be extrapolated for UiO-66-ox-Cu, although the theoretical loading was exceeded for one trial, suggesting copper impregnation may be occurring. Ammonia breakthrough experiments on UiO-66-$(COOCu)_2$ at various copper loadings show an inverse relation between ammonia capacity and metal content under both dry and wet conditions, attributed to steric effects blocking ammonia adsorption to the material. Analogous tests on UiO-66-ox-Cu indicate dry capacities increase almost linearly with copper loading, while wet loadings did not change

significantly due to adsorbent degradation in humid ammonia. Disparate loading and ammonia capture behavior between the two materials show the importance of copper carboxylate locations in MOFs for ammonia adsorption, and provide insight into engineering these functional groups onto similar materials for TIC removal.

Sample nanoporous materials are contrasted with the MOFs investigated here in Table 5 for their ammonia capacities, along with relative stabilities in humid conditions, to provide insight for current adsorption performances for materials on the vanguard of ammonia capture.

Table 5. Reported experimental dynamic ammonia capacities and water stability information for select adsorbents.

	NH_3 Dynamic Capacity (mmol g^{-1})		**Stability in Humid**
MOF	**Dry (0% RH)**	**Wet (80% RH)**	**NH_3 (Y/N)**
BPL Carbon[63]	0.17	0.29	Y
Zeolite Cu-Y[64]	4.92[a]	N/A	Y
Mg-MOF-74[63]	7.6	1.7	N
HKUST-1[65]	6.6	8.9	N
UiO-66-NH_2[41]	3.3	2.9	Y
Cu @ UiO-66	2.25	1.15	Y
UiO-66-ox-Cu	4.31	4.02	N
UiO-66-$(COOCu)_2$[28]	6.38	6.84	Y

[a] Breakthrough measurements taken between 0 kPa and 75 kPa

Results from this study give perspective onto the effects of engineering locations for copper carboxylate functionalities onto UiO-66 for ammonia adsorption. Linker

functionalized –COOCu groups on UiO-66-$(COOCu)_2$ appear to produce the highest potential for air purification applications on UiO-66 type materials. Furthermore, breakthrough experiments contrasting Cu @ UiO-66 and UiO-66-ox-Cu showed carboxyl functionalities to be necessary precursors for copper coordination to provide favorable ammonia uptake. Finally, variances in loading and ammonia capture behavior between UiO-66-$(COOCu)_2$ and UiO-66-ox-Cu through metal loading and subsequent ammonia breakthrough experiments show the impact of copper carboxylate locations and loadings for each system in ammonia adsorption, and provide insight for any future engineering of these functional groups onto sorbent materials for TIC removal.

4.2 Recommendations for Future Work

4.2.1 Elucidation of Copper Coordination Environment

The coordination environment of copper for all MOFs in this study was not ascertained. Understanding the coordination nature of copper in MOFs with high ammonia uptake performance would potentially help enable the engineering of specialized copper functionalities on future adsorbent for ammonia. Electron paramagnetic resonance (EPR)[66] was employed to probe the coordination nature of Cu in UiO-66-COOCu and UiO-66-$(COOCu)_2$, however definitive results on the bonding environment could not be attained. The extended X-ray adsorption fine structure (EXAFS) technique[67] has been used previously to find metal coordination nature in MOFs[13], and is a promising method for further characterizing the MOFs subjected to metal insertion in this work. Crystal structure refinement of the ordered structures using experimental X-ray

diffraction patterns of the MOFs could also be utilized to solve for atomic copper locations within the unit cell of the respective materials.[68] Some refinement work in solving these structures has already been accomplished, but higher resolution PXRD measurements are required for accurate fittings, and so this work is not presented here. DFT calculations have also been used to approximate metal locations in metal locations, such as transmetallation phenomena in MOF-5.[69]

4.2.2 Optimization of Copper Loading

Metal insertion conditions on UiO-66-ox-Cu were restricted to those used for UiO-66-COOCu and UiO-66-$(COOCu)_2$ to allow for comparison material properties throughout this study. However, the metal insertion procedure was temperature restricted due to the low thermal stabilities of the MOFs investigated by Garcia-Gutierrez, where it was found that increasing temperature increased copper loading.[28] Furthermore, concentration effects have not been investigated. The higher thermal stability of UiO-66-ox-Cu allows for further study on copper coordination conditions, where more extensive studies could be undertaken to optimize the copper loading on UiO-66-ox-Cu, and then investigate ammonia uptake performance. Furthermore, longer metal loading times could be used to expand on the kinetic studies performed on UiO-66-ox-Cu and UiO-66-$(COOCu)_2$ and optimize the metal loading on both materials.

4.2.3 Characterization and Control of Defects in UiO-66-vac/UiO-66-ox

The number of missing linker defects, though reproducible from gravimetric analyses, was not controlled for the synthesis of UiO-66-vac and UiO-66-ox. Rietveld or Pawley refinement of experimental X-ray diffraction data can potentially be used to solve

for the unit cell of the defective MOFs and provide greater insight into the textural properties of the materials, as well as further support carboxylic acid functionalization in UiO-66-ox. Control strategies via synthesis modulation can be used to control missing linker defects and subsequently carboxyl incorporation in UiO-66-ox to improve loading of functional groups used for ammonia capture.

4.2.4 Uptake Performance of Regenerated Materials Following TIC Exposure

The main purpose of the proposed material is to become incorporated into single-pass CBRN filters. However, reuse of adsorption media after TIC exposure is of pragmatic interest, as it would be more cost effective to use a material that can be regenerated after use, and retain high vapor uptake capacities for toxic gases for other air purification applications. Precedent for this testing exists in the literature, where certain Al based MOFs have shown such capabilities[70], and MIL-68 was reported to have been regenerated five times without significant loss in capacity for hydrogen sulfide adsorption[15]. The strategy commonly employed for these sorbents is to allow for regeneration through application of heat and vacuum.[4] Using these techniques, the regenerative properties for ammonia adsorption after multiple exposures can be ascertained for the MOFs investigated here to gauge their applicability for ammonia capture in air filtration processes that mandate reuse of sorbent material.

APPENDIX A

WET AMMONIA BREAKTHROUGH EXPERIMENTS on UiO-66-ox

Humid NH_3 breakthrough experiments were conducted on UiO-66-ox to determine uptake increases for UiO-66-ox-Cu following metal insertion. UiO-66-ox samples were activated in situ at 150 ℃ for 2 h under N_2 flow, and then allowed to cool before ammonia exposure. Humid breakthrough procedures are detailed in Section 2.3.

The breakthrough curve for humid ammonia uptake in UiO-66-ox is provided in Figure 26. An uptake of 2.30 mmol g^{-1} was calculated for this experiment, which is slightly less than the experimentally determined 2.5 mmol g^{-1} under dry NH_3 reported previously[33]. Slight decreases in uptake under humid streams have been reported for the similar UiO-66-COOH[28] and other UiO-66 systems[42], and this is attributed to competitive adsorption between water and ammonia species for adsorption sites. The shallow desorption curve indicates mass transfer resistance during nitrogen purging, which was similarly observed to be more prevalent under humid than dry conditions for materials tested in this work. BET surface area measurements should be conducted on the material before and after humid ammonia exposure to gauge any losses in porosity.

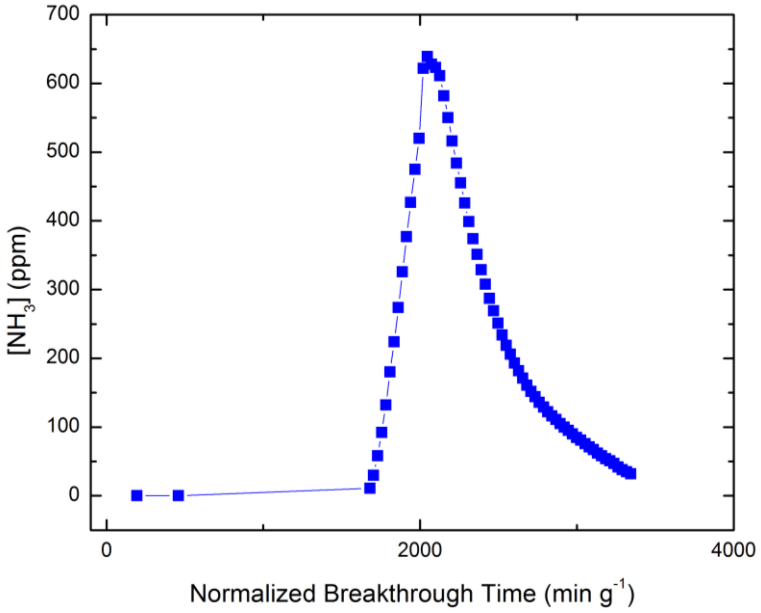

Figure 26. Humid ammonia breakthrough curve for UiO-66-ox

APPENDIX B

RAW DATA

B.1 WATER VAPOR SORPTION DATA

Table 6. Water vapor adsorption data for UiO-66-vac

Adsorption		Desorption	
RH (%)	Loading (mmol g^{-1})	RH (%)	Loading (mmol g^{-1})
0	0	89.35	33.22
10.68	3.81	79.51	32.78
20.53	6.16	59.86	31.19
30.36	15.14	40.19	27.50
40.19	24.85	20.53	6.43
50.02	29.84	0	2.12
59.86	31.22		
69.69	32.19		
79.50	32.76		
89.35	33.22		

Table 7. Water Vapor Adsorption Data for UiO-66-ox

Adsorption		Desorption	
RH (%)	Loading (mmol g^{-1})	RH (%)	Loading (mmol g^{-1})
0	0	89.34	15.48
10.68	0.13	79.49	15.14
20.52	3.69	59.85	13.97
30.36	5.18	40.20	8.01
40.18	6.42	20.54	5.74
50.02	8.20	0	2.95
59.85	10.84		
69.69	13.60		
79.51	14.68		
89.34	15.48		

Table 8. Water Vapor Adsorption Data for UiO-66-ox-Cu

Adsorption		Desorption	
RH (%)	Loading (mmol g^{-1})	RH (%)	Loading (mmol g^{-1})
0	0	89.34	20.37
10.69	2.02	79.49	20.06
20.53	3.59	59.85	18.42
30.36	5.13	40.19	9.65
40.19	6.51	20.54	5.11
50.02	11.21	0	2.99
59.86	15.89		
69.69	18.36		
79.50	19.78		
89.34	20.37		

Table 9. Water vapor adsorption data for UiO-66-COOH

Adsorption		Desorption	
RH (%)	Loading (mmol g^{-1})	RH (%)	Loading (mmol g^{-1})
0	0	89.33	9.74
10.69	0	79.49	9.57
20.53	0	59.85	8.03
30.36	0.77	40.20	3.88
40.19	2.50	20.53	0.93
50.02	3.98	0	0.32
59.85	6.14	--	--
69.69	7.54	--	--
79.49	9.45	--	--
89.33	9.74	--	--

Table 10. Water vapor adsorption data for UiO-66-$(COOH)_2$

Adsorption		Desorption	
RH (%)	Loading (mmol g^{-1})	RH (%)	Loading (mmol g^{-1})
0	0	89.34	6.64
10.70	0.01	79.50	6.70
20.53	0.11	59.85	5.38
30.36	2.38	40.19	3.80
40.19	3.54	20.54	0.98
50.03	4.22	0	0.44
59.86	4.98	--	--
69.67	5.88	--	--
79.49	6.65	--	--
89.34	6.64	--	--

B.2 Ammonia Breakthrough Data

Table 11. Dry ammonia breakthrough data for Cu @ UiO-66

Adsorption		Desorption	
Normalized time ($min\ g^{-1}$)	$[NH_3]$ (ppm)	Normalized time ($min\ g^{-1}$)	$[NH_3]$ (ppm)
0	0	2458.45	673
1603.33	10	2498.53	643
1616.70	16	2538.61	610
1656.78	37	2578.70	571
1696.86	61	2618.78	530
1736.95	86	2658.86	491
1777.03	117	2698.95	452
1817.11	147	2739.03	417
1857.20	175	2779.11	385
1897.28	206	2819.20	356
1937.36	234	2859.28	329
1977.45	262	2899.36	304
2017.53	292	2939.45	283
2057.61	322	2979.53	265
2097.70	351	3019.61	249
2137.78	383	3059.70	234
2177.86	412	3099.78	221
2217.95	443	3139.86	210
2258.03	476	3179.95	198
2298.11	510	3220.03	188
2338.20	599	3260.11	177
2378.28	665	3300.20	166
2418.36	684	3340.28	156
		3380.36	146
		3420.45	136
		3460.53	127
		3500.61	118
		3540.70	110

		3580.78	103
		3620.86	96
		3660.95	93
		3701.03	90
		3741.11	87
		3781.20	84
		3821.28	81
		3861.36	77
		3901.45	74
		3941.53	72
		3981.62	70
		4021.70	68
		4061.78	66
		4101.87	64
		4141.95	61
		4182.03	59
		4222.12	57
		4262.20	55
		4302.28	53
		4342.37	51
		4382.45	49
		4422.53	47
		4462.62	45
		4502.70	43
		4542.78	41
		4582.87	39
		4622.95	37
		4663.03	35
		4703.12	33
		4743.20	31
		4783.28	29
		4823.37	27
		4863.45	25
		4903.53	24

		4943.62	23
		4983.70	22
		5023.78	21
		5063.87	20
		5103.95	19
		5144.03	18
		5184.12	17
		5224.20	16
		5264.28	15
		5304.37	14
		5344.45	13
		5384.53	12

Table 12. Dry ammonia breakthrough data for UiO-66-ox-Cu

Adsorption		Desorption	
Normalized time ($min\ g^{-1}$)	$[NH_3]$ (ppm)	Normalized time ($min\ g^{-1}$)	$[NH_3]$ (ppm)
67.89	0	549.30	659
160.47	0	558.56	600
253.05	0	567.82	549
283.91	0	577.08	502
447.46	21	586.33	461
456.72	70	595.59	424
465.98	132	604.85	390
475.24	200	614.11	360
484.50	269	623.36	332
493.75	337	632.62	307
503.01	407	641.88	284
512.27	479	651.14	264
521.53	567	660.40	245
530.79	703	669.65	227
540.04	711	678.91	213

		688.17	199
		697.43	186
		706.69	174
		715.94	164
		725.20	154
		734.46	144
		743.72	136
		752.97	128
		762.23	121
		771.49	115
		780.75	109
		790.01	103
		799.26	98
		808.52	93
		817.78	88
		827.04	84
		836.30	80
		845.55	76
		854.81	72
		864.07	68
		873.33	64
		882.59	60
		891.84	57
		901.10	54
		910.36	51
		919.62	48
		928.87	45
		938.13	42
		947.39	39
		956.65	36
		965.91	34
		975.16	32
		984.42	30
		993.68	28

		1002.94	26
		1012.20	24
		1021.45	22
		1030.71	20

Table 13. Wet ammonia breakthrough data for UiO-66-ox

Adsorption		Desorption	
Normalized time ($min\ g^{-1}$)	$[NH_3]$ (ppm)	Normalized time ($min\ g^{-1}$)	$[NH_3]$ (ppm)
194.00	0	2072.31	628
458.55	0	2098.77	623
1679.72	11	2125.22	611
1701.94	30	2151.68	582
1728.40	58	2178.13	550
1754.85	92	2204.59	516
1781.31	132	2231.04	484
1807.76	180	2257.50	455
1834.22	224	2283.95	426
1860.67	274	2310.41	399
1887.13	326	2336.86	374
1913.58	377	2363.32	351
1940.04	427	2389.77	329
1966.49	475	2416.23	308
1992.95	520	2442.68	287
2019.40	622	2469.14	269
2045.86	639	2495.59	251
		2522.05	234
		2548.50	219
		2574.96	206
		2601.41	193
		2627.87	182
		2654.32	171
		2680.78	161

		2707.23	152
		2733.69	144
		2760.14	136
		2786.60	129
		2813.05	122
		2839.51	116
		2865.96	111
		2892.42	105
		2918.87	100
		2945.33	95
		2971.78	90
		2998.24	85
		3024.69	81
		3051.15	76
		3077.60	71
		3104.06	67
		3130.51	62
		3156.97	58
		3183.42	54
		3209.88	51
		3236.33	47
		3262.79	42
		3289.24	38
		3315.70	35
		3342.15	32

Table 14. Humid ammonia breakthrough data for Cu @ UiO-66

Adsorption		Desorption	
Normalized time (min g^{-1})	[NH_3] (ppm)	Normalized time (min g^{-1})	[NH_3] (ppm)
0	0	1229.41	638
824.52	10	1240.46	627

831.88	17	1251.50	608
842.92	29	1262.54	584
853.96	42	1273.59	556
865.01	58	1284.63	526
876.05	75	1295.67	496
887.09	94	1306.71	467
898.14	113	1317.76	441
909.18	132	1328.80	418
920.22	151	1339.84	398
931.26	169	1350.88	379
942.31	187	1361.93	363
953.35	205	1372.97	346
964.39	221	1384.01	324
975.43	238	1395.05	301
986.48	255	1406.10	280
997.52	273	1417.14	263
1008.56	290	1428.18	247
1019.60	309	1439.22	234
1030.65	327	1450.27	222
1041.69	345	1461.31	213
1052.73	362	1472.35	204
1063.77	381	1483.40	196
1074.82	397	1494.44	188
1085.86	412	1505.48	179
1096.90	427	1516.52	172
1107.95	439	1527.57	163
1118.99	451	1538.61	155
1130.03	462	1549.65	147
1141.07	473	1560.69	141
1152.12	482	1571.74	134
1163.16	491	1582.78	127
1174.20	500	1593.82	121
1185.24	530	1604.86	115
1196.29	574	1615.91	111

1207.33	630	1626.95	107
1218.37	640	1637.99	103
		1649.04	100
		1660.08	96
		1671.12	91

Table 15. Humid ammonia breakthrough data for UiO-66-ox-Cu

Adsorption		Desorption	
Normalized time (min g^{-1})	[NH_3] (ppm)	Normalized time (min g^{-1})	[NH_3] (ppm)
271.60	0	3530.86	607
641.98	0	3567.90	584
1012.35	0	3604.94	559
1135.80	0	3641.98	537
2370.37	0	3679.01	522
2880.25	10	3716.05	504
2901.23	18	3753.09	475
2938.27	33	3790.12	443
2975.31	52	3827.16	410
3012.35	77	3864.20	377
3049.38	108	3901.23	348
3086.42	141	3938.27	321
3123.46	178	3975.31	295
3160.49	218	4012.35	272
3197.53	259	4049.38	252
3234.57	302	4086.42	233
3271.60	343	4123.46	216
3308.64	385	4160.49	201
3345.68	424	4197.53	186
3382.72	464	4234.57	173
3419.75	499	4271.60	162
3456.79	551	4308.64	151

3493.83	620	4345.68	141
		4382.72	132
		4419.75	123
		4456.79	115
		4493.83	108
		4530.86	101
		4567.90	95
		4604.94	80
		4641.98	70
		4679.01	65
		4716.05	60
		4753.09	54
		4790.12	49
		4827.16	42
		4864.20	40
		4901.23	37
		4938.27	34
		4975.31	30
		5012.35	28
		5049.38	27
		5086.42	25
		5123.46	23
		5160.49	21
		5197.53	20
		5234.57	18
		5271.60	16
		5308.64	15
		5345.68	14
		5382.72	13
		5419.75	11
		5456.79	8
		5493.83	6
		5530.86	6
		5567.90	5

		5604.94	4
		5641.98	3
		5679.01	2
		5716.05	1
		5753.09	1
		5790.12	1
		5827.16	1
		5864.20	0

Table 16. Dry ammonia breakthrough data for UiO-66-$(COOCu)_2$ – 6h

Adsorption		Desorption	
Normalized time ($min\ g^{-1}$)	$[NH_3]$ (ppm)	Normalized time ($min\ g^{-1}$)	$[NH_3]$ (ppm)
279.90	0	2684.48	544
661.58	0	2722.65	499
1043.26	0	2760.81	461
1424.94	0	2798.98	428
1806.62	0	2837.15	396
2059.80	12	2875.32	366
2073.79	18	2913.49	338
2111.96	36	2951.65	312
2150.13	59	2989.82	287
2188.30	84	3027.99	264
2226.46	113	3066.16	243
2264.63	143	3104.33	225
2302.80	177	3142.49	208
2340.97	214	3180.66	193
2379.13	252	3218.83	179
2417.30	291	3257.00	165
2455.47	329	3295.17	154
2493.64	368	3333.33	144
2531.81	407	3371.50	135

2569.97	444	3409.67	126
2608.14	508	3447.84	119
2646.31	574	3486.01	112
		3524.17	107
		3562.34	101
		3600.51	96
		3638.68	91
		3676.84	87
		3715.01	82
		3753.18	79
		3791.35	75
		3829.52	72
		3867.68	68
		3905.85	65
		3944.02	62
		3982.19	59
		4020.36	56
		4058.52	54
		4096.69	51
		4134.86	49
		4173.03	47
		4211.20	45
		4249.36	43
		4287.53	41
		4325.70	40

Table 17. Humid ammonia breakthrough data for UiO-66-$(COOCu)_2$ – 6h

Adsorption		Desorption	
Normalized time ($min\ g^{-1}$)	$[NH_3]$ (ppm)	Normalized time ($min\ g^{-1}$)	$[NH_3]$ (ppm)
333.33	0	3787.88	501
787.88	0	3833.33	471

1242.42	0	3878.79	440
1696.97	0	3924.24	413
2151.52	0	3969.70	391
2909.09	0	4015.15	378
3045.15	10	4060.61	360
3060.61	16	4106.06	327
3106.06	31	4151.52	295
3151.52	50	4196.97	265
3196.97	72	4242.42	241
3242.42	96	4287.88	219
3287.88	122	4333.33	200
3333.33	152	4378.79	183
3378.79	184	4424.24	169
3424.24	219	4469.70	153
3469.70	253	4515.15	142
3515.15	289	4560.61	130
3560.61	324	4606.06	119
3606.06	358	4651.52	109
3651.52	390	4696.97	100
3696.97	448	4742.42	91
3742.42	515	4787.88	83
		4833.33	78
		4878.79	72
		4924.24	66
		4969.70	63
		5015.15	57
		5060.61	55
		5106.06	51
		5151.52	48
		5196.97	45
		5242.42	42
		5287.88	40
		5333.33	34
		5378.79	32

		5424.24	27
		5469.70	23
		5515.15	16
		5560.61	15
		5606.06	15

Table 18. Dry ammonia breakthrough data for UiO-66-ox-Cu – 6h

Adsorption		Desorption	
Normalized time ($min\ g^{-1}$)	$[NH_3]$ (ppm)	Normalized time ($min\ g^{-1}$)	$[NH_3]$ (ppm)
338.41	0	2673.43	643
846.02	0	2724.20	603
1353.64	0	2774.96	558
1522.84	0	2825.72	512
1817.29	12	2876.48	469
1861.25	27	2927.24	428
1912.01	51	2978.00	389
1962.77	79	3028.76	353
2013.54	108	3079.53	322
2064.30	139	3130.29	293
2115.06	172	3181.05	267
2165.82	206	3231.81	243
2216.58	242	3282.57	222
2267.34	280	3333.33	204
2318.10	321	3384.09	187
2368.87	363	3434.86	172
2419.63	408	3485.62	159
2470.39	453	3536.38	147
2521.15	528	3587.14	137
2571.91	631	3637.90	127
2622.67	662	3688.66	119
		3739.42	111

		3790.19	105
		3840.95	98
		3891.71	92
		3942.47	86
		3993.23	81
		4043.99	75
		4094.75	71
		4145.52	67
		4196.28	63
		4247.04	59
		4297.80	55
		4348.56	52
		4399.32	50

Table 19. Humid ammonia breakthrough data for UiO-66-ox-Cu – 6h

Adsorption		Desorption	
Normalized time ($min\ g^{-1}$)	$[NH_3]$ (ppm)	Normalized time ($min\ g^{-1}$)	$[NH_3]$ (ppm)
261.90	0	3226.19	585
619.05	0	3261.90	550
976.19	0	3297.62	520
1095.24	0	3333.33	496
1333.33	0	3369.05	476
1690.48	0	3404.76	461
2285.71	0	3440.48	448
2797.62	14	3476.19	429
2833.33	49	3511.90	402
2869.05	93	3547.62	374
2904.76	139	3583.33	347
2940.48	188	3619.05	324
2976.19	239	3654.76	302
3011.90	292	3690.48	282

3047.62	346	3726.19	264
3083.33	397	3761.90	248
3119.05	447	3797.62	234
3154.76	525	3833.33	221
3190.48	611	3869.05	209
		3904.76	197
		3940.48	187
		3976.19	177
		4011.90	168
		4047.62	159
		4083.33	150
		4119.05	141
		4154.76	131
		4190.48	123
		4226.19	114
		4261.90	105
		4297.62	98
		4333.33	91
		4369.05	84
		4404.76	78
		4440.48	73
		4476.19	69
		4511.90	64
		4547.62	60
		4583.33	57
		4619.05	53
		4654.76	51
		4690.48	47
		4726.19	45
		4761.90	42
		4797.62	40
		4833.33	34
		4869.05	30
		4904.76	26

		4940.48	22
		4976.19	19
		5011.90	17
		5047.62	15
		5083.33	13
		5119.05	12
		5154.76	12
		5190.48	0

Table 20. Dry ammonia breakthrough data for UiO-66-$(COOCu)_2$ – 12h

Adsorption		Desorption	
Normalized time ($min\ g^{-1}$)	$[NH_3]$ (ppm)	Normalized time ($min\ g^{-1}$)	$[NH_3]$ (ppm)
251.95	0	2292.77	583
629.88	0	2330.56	526
1007.81	0	2368.35	475
1385.74	0	2406.15	430
1763.67	0	2443.94	389
1855.63	12	2481.73	353
1877.05	23	2519.53	321
1914.84	49	2557.32	291
1952.63	86	2595.11	266
1990.43	131	2632.91	243
2028.22	182	2670.70	223
2066.01	238	2708.49	205
2103.80	300	2746.28	189
2141.60	363	2784.08	176
2179.39	428	2821.87	164
2217.18	534	2859.66	153
2254.98	620	2897.46	143
		2935.25	134
		2973.04	126

		3010.83	119
		3048.63	112
		3086.42	105
		3124.21	99
		3162.01	94
		3199.80	89
		3237.59	84
		3275.38	79
		3313.18	75
		3350.97	71
		3388.76	67
		3426.56	64
		3464.35	60
		3502.14	58
		3539.93	56
		3577.73	53
		3615.52	51
		3653.31	50
		3691.11	49
		3728.90	46
		3766.69	44

Table 21. Humid ammonia breakthrough data for UiO-66-$(COOCu)_2$ – 12h

Adsorption		Desorption	
Normalized time ($min\ g^{-1}$)	$[NH_3]$ (ppm)	Normalized time ($min\ g^{-1}$)	$[NH_3]$ (ppm)
291.01	0	4298.94	483
687.83	0	4338.62	465
1084.66	0	4378.31	451
1481.48	0	4417.99	443
1878.31	0	4457.67	430
2539.68	0	4497.35	403

3035.69	11	4537.04	368
3068.78	15	4576.72	330
3108.47	20	4616.40	301
3148.15	27	4656.08	274
3187.83	34	4695.77	248
3227.51	41	4735.45	227
3267.20	49	4775.13	208
3306.88	59	4814.81	191
3346.56	69	4854.50	161
3386.24	78	4894.18	146
3425.93	90	4933.86	134
3465.61	102	4973.54	122
3505.29	114	5013.23	112
3544.97	127	5052.91	102
3584.66	140	5092.59	94
3624.34	153	5132.28	87
3664.02	167	5171.96	80
3703.70	182	5211.64	74
3743.39	197	5251.32	69
3783.07	213	5291.01	64
3822.75	230	5330.69	60
3862.43	252	5370.37	57
3902.12	274	5410.05	54
3941.80	289	5449.74	50
3981.48	310	5489.42	47
4021.16	332	5529.10	42
4060.85	354	5568.78	40
4100.53	376	5608.47	34
4140.21	397	5648.15	30
4179.89	425	5687.83	26
4219.58	496	5727.51	22
4259.26	498	5767.20	19
		5806.88	17
		5846.56	15

		5886.24	13
		5925.93	12
		5965.61	12
		6005.29	0

Table 22. Dry ammonia breakthrough data for UiO-66-ox-Cu – 12h

Adsorption		Desorption	
Normalized time ($min\ g^{-1}$)	$[NH_3]$ (ppm)	Normalized time ($min\ g^{-1}$)	$[NH_3]$ (ppm)
281.29	0	4331.93	588
703.23	0	4374.12	562
1125.18	0	4416.32	540
1265.82	0	4458.51	519
2672.29	0	4500.70	498
3729.99	11	4542.90	478
3741.21	16	4585.09	456
3783.40	35	4627.29	429
3825.60	60	4669.48	398
3867.79	90	4711.67	368
3909.99	130	4753.87	341
3952.18	165	4796.06	315
3994.37	208	4838.26	293
4036.57	252	4880.45	272
4078.76	298	4922.64	254
4120.96	344	4964.84	239
4163.15	388	5007.03	223
4205.34	431	5049.23	211
4247.54	480	5091.42	199
4289.73	592	5133.61	186
		5175.81	174
		5218.00	162
		5260.20	150
		5302.39	140

		5344.59	130
		5386.78	121
		5428.97	112
		5471.17	104
		5513.36	97
		5555.56	90
		5597.75	84
		5639.94	79
		5682.14	74
		5724.33	70
		5766.53	66
		5808.72	63
		5850.91	59
		5893.11	56
		5935.30	53
		5977.50	50

Table 23. Humid ammonia breakthrough data for UiO-66-ox-Cu – 12h

Adsorption		Desorption	
Normalized time ($min\ g^{-1}$)	$[NH_3]$ (ppm)	Normalized time ($min\ g^{-1}$)	$[NH_3]$ (ppm)
273.63	0	2810.95	522
646.77	0	2848.26	491
1019.90	0	2885.57	462
1144.28	0	2922.89	441
1766.17	0	2960.20	424
2258.71	11	2997.51	397
2288.56	27	3034.83	367
2325.87	48	3072.14	338
2363.18	77	3109.45	313
2400.50	107	3146.77	289
2437.81	141	3184.08	268

2475.12	178	3221.39	248
2512.44	216	3258.71	229
2549.75	256	3296.02	212
2587.06	297	3333.33	195
2624.38	337	3370.65	179
2661.69	376	3407.96	165
2699.00	414	3445.27	153
2736.32	460	3482.59	142
2773.63	547	3519.90	132
		3557.21	122
		3594.53	113
		3631.84	104
		3669.15	97
		3706.47	90
		3743.78	83
		3781.09	77
		3818.41	72
		3855.72	67
		3893.03	63
		3930.35	58
		3967.66	54
		4004.98	51
		4042.29	49
		4079.60	45
		4116.92	42
		4154.23	39

REFERENCES

1. Jacoby, M. Air Filters for the Face. *C&EN Chicago* **2014**, 34–38.

2. Karasik, T. Toxic Warfare. *RAND*: Santa Monica, CA, 2002.

3. Britt, D.; Tranchemontagne, D.; Yaghi, O. M. Metal-Organic Frameworks with High Capacity and Selectivity for Harmful Gases. *Proc. Natl. Acad. Sci. U. S. A.* **2008**, *105*, 11623–11627.

4. Filtration and Air-Cleaning Systems to Protect Building Environments from Airborne Chemical, Biological, or Radiological Attacks. *Department of Health and Human Services*, 2003

5. Chemical Sampling Information: Ammonia https://www.osha.gov/dts/chemicalsampling/data/CH_218300.html (accessed Mar 8, 2016).

6. West Fertilzer Company Fire and Explosion. *United States Chemical Safety and Hazard Investigation Board*, 2013.

7. Sherlock, R. Syria chemical weapons: Britain calls for urgent investigation http://www.telegraph.co.uk/news/worldnews/middleeast/syria/10797723/Syria-chemical-weapons-Britain-calls-for-urgent-investigation.html (accessed Mar 3, 2016).

8. Yaghi, O.; O'Keeffe, M.; Ockwig, N. Reticular Synthesis and the Design of New Materials. *Nature* **2003,** *423*, 705-714.

9. Furukawa, H.; Cordova, K. E.; O'Keeffe, M.; Yaghi, O. M. The Chemistry and Applications of Metal-Organic Frameworks. *Science* **2013**, *341*, 1230444–1 – 1230444–12.

10. Costa, J. S.; Gamez, P.; Black, C. a.; Roubeau, O.; Teat, S. J.; Reedijk, J. Chemical Modification of a Bridging Ligand inside a Metal-Organic Framework While Maintaining the 3D Structure. *Eur. J. Inorg. Chem.* **2008**, 1551–1554.

11. Demessence, A.; D'Alessandro, D. M.; Foo, M. L.; Long, J. R. Strong CO_2 Binding in a Water-Stable, Triazolate-Bridged Metal-Organic Framework Functionalized with Ethylenediamine. *J. Am. Chem. Soc.* **2009**, *131*, 8784–8786.

12. Jiang, J.; Yaghi, O. M. Brønsted Acidity in Metal–Organic Frameworks. *Chem. Rev.* **2015**, 6966–6997.

13. Stock, N.; Biswas, S. Synthesis of Metal-Organic Frameworks (MOFs): Routes to Various MOF Topologies, Morphologies, and Composites. *Chem. Rev.* **2012**, *112*, 933–969.

14. Ragon, F.; Campo, B.; Yang, Q.; Martineau, C.; Wiersum, A. D.; Lago, A.; Guillerm, V.; Hemsley, C.; Eubank, J. F.; Vishnuvarthan, M.; *et al.* Acid-Functionalized UiO-66(Zr) MOFs and Their Evolution after Intra-Framework Cross-Linking: Structural Features and Sorption Properties. *J. Mater. Chem. A* **2015**, *3*, 3294–3309.

15. DeCoste, J. B.; Peterson, G. W. Metal − Organic Frameworks for Air Purification of Toxic Chemicals. *Chem. Rev.* **2014**, 5695−5727.

16. Wilcox, O.; Katsoulidis, A.; Fateeva, A.; Smith, M.; Stone, C. A.; Rosseinsky, M. J. Acid Loaded Porphyrin-Based Metal-Organic Framework for Ammonia Uptake. *Chem. Commun.* **2015**, *4*, 1166–1169.

17. Petit, C.; Mendoza, B.; Bandosz, T. J. Reactive Adsorption of Ammonia on Cu-Based MOF/graphene Composites. *Langmuir* **2010**, *26*, 15302–15309.

18. Nijem, N.; Fürsich, K.; Bluhm, H.; Leone, S. R.; Gilles, M. K. Ammonia Adsorption and Co-Adsorption with Water in HKUST-1: Spectroscopic Evidence for Cooperative Interactions. *J. Phys. Chem. C* **2015**, *119*, 24781–24788.

19. Bashkova, S.; Bandosz, T. J. Journal of Colloid and Interface Science Effect of Surface Chemical and Structural Heterogeneity of Copper-Based MOF / Graphite Oxide Composites on the Adsorption of Ammonia. *J. Colloid Interface Sci.* **2014**, *417*, 109–114.

20. Schoenecker, P. M.; Carson, C. G.; Jasuja, H.; Flemming, C. J. J.; Walton, K. S. Effect of Water Adsorption on Retention of Structure and Surface Area of Metal–Organic Frameworks. *Ind. Eng. Chem. Res.* **2012**, *51*, 6513–6519.

21. Cavka, J. H.; Jakobsen, S.; Olsbye, U.; Guillou, N.; Lamberti, C.; Bordiga, S.; Lillerud, K. P. A New Zirconium Inorganic Building Brick Forming Metal Organic Frameworks with Exceptional Stability. *J. Am. Chem. Soc.* **2008**, *130*, 13850–13851.

22. Valenzano, L.; Civalleri, B.; Chavan, S.; Bordiga, S.; Nilsen, M. H.; Jakobsen, S.; Lillerud, K. P.; Lamberti, C. Disclosing the Complex Structure of UiO-66 Metal Organic Framework: A Synergic Combination of Experiment and Theory. *Chem. Mater.* **2011**, *23*, 1700–1718.

23. Morris, W.; Doonan, C. J.; Yaghi, O. M. Postsynthetic Modification of a Metal-Organic Framework for Stabilization of a Hemiaminal and Ammonia Uptake. *Inorg. Chem.* **2011**, *50*, 6853–6855.

24. Hou, J.; Luan, Y.; Tang, J.; Wensley, A. M.; Yang, M.; Lu, Y. Synthesis of UiO-66-NH_2 Derived Heterogeneous Copper (II) Catalyst and Study of Its Application in the Selective Aerobic Oxidation of Alcohols. *J. Mol. Catal. A Chem.* **2015**, *407*, 53–59.

25. Getman, R. B.; Miller, J. H.; Wang, K.; Snurr, R. Q. Metal Alkoxide Functionalization in Metal-Organic Frameworks for Enhanced Ambient-Temperature Hydrogen Storage. *J. Phys. Chem. C* **2011**, *115*, 2066–2075.

26. Kim, M. H.; Cho, I. H.; Park, J. H.; Choi, S. O.; Lee, I.-S. Adsorption of CO_2 and CO on H-Zeolites with Different Framework Topologies and Chemical Compositions and a Correlation to Probing Protonic Sites Using NH3 Adsorption. *J. Porous Mater.* **2016**, *23*, 291–299.

27. Kim, K. C.; Moghadam, P. Z.; Fairen-Jimenez, D.; Snurr, R. Q. Computational Screening of Metal Catecholates for Ammonia Capture in Metal–Organic Frameworks. *Langmuir* **2013**, *29*, 1446-1456.

28. Garcia-Gutierrez, E. Copper Insertion in a Series of Metal-Organic Frameworks with Uncoordinated Carboxylic Acid Groups for Ammonia Removal. M.S. Thesis. Georgia Institute of Technology **2015**.

29. Jasuja, H. Developing Design Criteria and Scale-Up Methods for Water-Stable Metal-Organic Frameworks for Adsorption Applications. Ph.D. Dissertation. Georgia Institute of Technology 2014.

30. Cliffe, M. J.; Wan, W.; Zou, X.; Chater, P. a; Kleppe, A. K.; Tucker, M. G.; Wilhelm, H.; Funnell, N. P.; Coudert, F.-X.; Goodwin, A. L. Correlated Defect Nanoregions in a Metal-Organic Framework. *Nat. Commun.* **2014**, *5*, 4176.

31. Ghosh, P.; Colón, Y. J.; Snurr, R. Q. Water Adsorption in UiO-66: The Importance of Defects. *Chem. Commun.* **2014**, *50*, 11329–11331.

32. Katz, M. J.; Brown, Z. J.; Colón, Y. J.; Siu, P. W.; Scheidt, K. a; Snurr, R. Q.; Hupp, J. T.; Farha, O. K. A Facile Synthesis of UiO-66, UiO-67 and Their Derivatives. *Chem. Commun. (Camb).* **2013**, *49*, 9449–9451.

33. DeCoste, J. B.; Demasky, T. J.; Katz, M. J.; Farha, O. K.; Hupp, J. T. A UiO-66 Analogue with Uncoordinated Carboxylic Acids for the Broad-Spectrum Removal of Toxic Chemicals. *New J. Chem.* **2015**, *39*, 2396–2399.

34. López-Maya, E.; Montoro, C.; Rodríguez-Albelo, L. M.; Aznar Cervantes, S. D.; Lozano-Pérez, A. A.; Cenís, J. L.; Barea, E.; Navarro, J. A. R. Textile/Metal-Organic-Framework Composites as Self-Detoxifying Filters for Chemical-Warfare Agents. *Angew. Chemie Int. Ed.* **2015**, *54*, 6790–6794.

35. Biswas, S.; Van Der Voort, P. A General Strategy for the Synthesis of Functionalised UiO-66 Frameworks: Characterisation, Stability and CO_2 Adsorption Properties. *Eur. J. Inorg. Chem.* **2013**, 2154–2160.

36. Tulig, K.; Walton, K. S. An Alternative UiO-66 Synthesis for HCl-Sensitive Nanoparticle Encapsulation. *RSC Adv.* **2014**, *4*, 51080–51083.

37. Guo, Z.; Xiao, C.; Maligal-Ganesh, R. V.; Zhou, L.; Goh, T. W.; Li, X.; Tesfagaber, D.; Thiel, A.; Huang, W. Pt Nanoclusters Confined within Metal–Organic Framework Cavities for Chemoselective Cinnamaldehyde Hydrogenation. *ACS Catal.* **2014**, *4*, 1340–1348.

38. Walton, K. S.; Snurr, R. Q.; K.S. Walton, R. Q. S. Applicability of the BET Method for Determining Surface Areas of Microporous Metal-Organic Frameworks. *J. Am. Chem. Soc.* **2007**, *129*, 8552–8556.

39. Gómez-Gualdrón, D. A.; Moghadam, P. Z.; Hupp, J. T.; Farha, O. K.; Snurr, R. Q. Application of Consistency Criteria To Calculate BET Areas of Micro- And Mesoporous Metal–Organic Frameworks. *J. Am. Chem. Soc.* **2015**, *138*, 215–224.

40. Mangarella, M. C.; Walton, K. S. Tailored Fe3C-Derived Carbons with Embedded Fe Nanoparticles for Ammonia Adsorption. *Carbon N. Y.* **2015**, *95*, 208–219.

41. Peterson, G. W.; DeCoste, J. B.; Fatollahi-Fard, F.; Britt, D. K. Engineering UiO-66-NH_2 for Toxic Gas Removal. *Ind. Eng. Chem. Res.* **2014**, *53*, 701–707.

42. Jasuja, H.; Peterson, G. W.; Decoste, J. B.; Browe, M. a.; Walton, K. S. Evaluation of MOFs for Air Purification and Air Quality Control Applications: Ammonia Removal from Air. *Chem. Eng. Sci.* **2015**, *124*, 118–124.

43. Sabo, M.; Henschel, A.; Fröde, H.; Klemm, E.; Kaskel, S. Solution Infiltration of Palladium into MOF-5: Synthesis, Physisorption and Catalytic Properties. *J. Mater. Chem.* **2007**, *17*, 3827.

44. Toxicological Profile for Copper. U.S. Department of Health and Human Services. Agency for Toxic Substances and Disease Registry. 2002. http://www.atsdr.cdc.gov/toxprofiles/tp126.pdf, accessed on 01/21/2016.

45. Garibay, S. J.; Cohen, S. M. Isoreticular Synthesis and Modification of Frameworks with the UiO-66 Topology. *Chem. Commun. (Camb).* **2010**, *46*, 7700–7702.

46. Ameloot, R.; Aubrey, M.; Wiers, B. M.; Gõmora-Figueroa, A. P.; Patel, S. N.; Balsara, N. P.; Long, J. R. Ionic Conductivity in the Metal-Organic Framework UiO-66 by Dehydration and Insertion of Lithium Tert-Butoxide. *Chem. - A Eur. J.* **2013**, *19*, 5533–5536.

47. Lin, K.-Y. A.; Chen, S.-Y.; Jochems, A. P. Zirconium-Based Metal Organic Frameworks: Highly Selective Adsorbents for Removal of Phosphate from Water and Urine. *Mater. Chem. Phys.* **2015**, *160*, 168–176.

48. Shi, M.; Li, Z.; Yuan, Y.; Yue, T.; Wang, J.; Li, R.; Chen, J. In Situ Oxidized Magnetite Membranes from 316L Porous Stainless Steel via a Two-Stage Sintering Process for Hexavalent Chromium [Cr(VI)] Removal from Aqueous Solutions. *Chem. Eng. J.* **2015**, *265*, 84–92.

49. Burtch, N. C.; Jasuja, H.; Walton, K. S. Water Stability and Adsorption in Metal-Organic Frameworks. *Chem. Rev.* **2014**, *114*, 10575–10612.

50. Moghadam, P. Z.; Fairen-Jimenez, D.; Snurr, R. Q. Efficient Identification of Hydrophobic MOFs: Application in the Capture of Toxic Industrial Chemicals. *J. Mater. Chem. A.* **2016**, *4*, 529–536.

51. Schoenecker, P. M. High-Throughput Synthesis and Application Development of Water-Stable MOFs. Ph.D. Dissertation. Georgia Institute of Technology **2012**.

52. Sing, K. S. W.; Everett, D. H.; Haul, R. a. W.; Moscou, L.; Pierotti, R. a.; Rouquérol, J.; Siemieniewska, T. Reporting Physisorption Data for Gas/Solid Systems with Special Reference to the Determination of Surface Area and Porosity. *Pure Appl. Chem.* **1982**, *54*, 2201–2218.

53. Low, J. J.; Jakubczak, P.; Abrahamian, J. F.; Faheem, S. A.; Willis, R. R. Virtual High Throughput Screening Confirmed Experimentally : Porous Coordination Polymer Hydration. *J. Am. Chem. Soc.* **2009**, *131*, 15834–15842.

54. Hu, Z.; Peng, Y.; Kang, Z.; Qian, Y.; Zhao, D. A Modulated Hydrothermal (MHT) Approach for the Facile Synthesis of UiO-66-Type MOFs. *Inorg. Chem.* **2015**, *54*, 4862–4868.

55. Mulfort, K. L.; Farha, O. K.; Stern, C. L.; Sarjeant, A. A.; Hupp, J. T. Post-Synthesis Alkoxide Formation Within Metal Organic Framework Materials : A Strategy for Incorporating Highly Coordinatively Unsaturated Metal Ions. *J. Am. Chem. Soc.* **2009**, *131*, 3866–3868.

56. Khazraei Vizhemehr, A.; Haghighat, F.; Lee, C. S. Gas-Phase Filters Breakthrough Models at Low Concentration - Effectof Relative Humidity. *Build. Environ.* **2014**, *75*, 1–10.

57. Otero, V.; Sanches, D.; Montagner, C.; Vilarigues, M.; Carlyle, L.; Lopes, J. A.; Melo, M. J. Characterisation of Metal Carboxylates by Raman and Infrared Spectroscopy in Works of Art. *J. Raman Spectrosc.* **2014**, *45*, 1197–1206.

58. Trickett, C. a.; Gagnon, K. J.; Lee, S.; Gándara, F.; Bürgi, H.-B.; Yaghi, O. M. Definitive Molecular Level Characterization of Defects in UiO-66 Crystals. *Angew. Chemie Int. Ed.* **2015**, 11162–11167.

59. Petit, C. Factors Affecting the Removal of Ammonia from Air on Carbonaceous Materials: Investigation of Reactive Adsorption Mechanism. Springer 2012.

60. Watanabe, T.; Sholl, D. S. Molecular Chemisorption on Open Metal Sites in Cu_3 (Benzenetricarboxylate)$_2$: A Spatially Periodic Density Functional Theory Study. *J. Chem. Phys.* **2010**, *133*, 094509-1 - 094509-13.

61. Yu, D.; Ghosh, P.; Snurr, R. Q. Hierarchical Modeling of Ammonia Adsorption in Functionalized Metal–organic Frameworks. *Dalt. Trans.* **2012**, *41*, 3962.

62. Soubeyrand-Lenoir, E.; Vagner, C.; Yoon, J. W.; Bazin, P.; Ragon, F.; Hwang, Y. K.; Serre, C.; Chang, J.; Llewellyn, P. L. How Water Fosters a Remarkable 5-Fold Increase in Low-Pressure CO_2 Uptake within Mesoporous MIL-100(Fe). *J. Am. Chem. Soc.* **2012**, *134*, 10174–10181.

63. Grant Glover, T.; Peterson, G. W.; Schindler, B. J.; Britt, D.; Yaghi, O. MOF-74 Building Unit Has a Direct Impact on Toxic Gas Adsorption. *Chem. Eng. Sci.* **2011**, *66*, 163–170.

64. Liu, C. Y.; Aika, K. I. Ammonia Adsorption on Ion Exchanged Y-Zeolites as Ammonia Storage Material. *J. Japan Pet. Inst.* **2003**, *46*, 301–307.

65. Peterson, G. W.; Wagner, G. W.; Balboa, A.; Mahle, J.; Sewell, T.; Karwacki, C. J. Ammonia Vapor Removal by Cu_3 $(BTC)_2$ and Its Characterization by MAS NMR. *J. Phys. Chem. C. Nanomater. Interfaces* **2009**, *113*, 13906–13917.

66. Junk, M. J. N. Electron Paramagnetic Resonance Theory. *Assess. Funct. Struct. Mol. Transp. by EPR Spectrosc.* **2012**, 1–42.

67 Newville, M. Fundamentals of XAFS. Consortium for Advanced Radiation Sources. University of Chicago 2004.

68. Basic X-Ray Powder Diffraction. http://xray.tamu.edu/pdf/notes/intro2xrd.pdf, accessed on 10/13/2015.

69. Bellarosa, L.; Brozek, C. K.; Garc á-Melchor, M.; Dincă, M.; López, N. When the Solvent Locks the Cage: Theoretical Insight into the Transmetalation of MOF-5 Lattices and Its Kinetic Limitations. *Chem. Mater.* **2015**, *27*, 3422–3429.

70. Kajiwara, T.; Higuchi, M.; Watanabe, D.; Higashimura, H.; Yamada, T.; Kitagawa, H. A Systematic Study on the Stability of Porous Coordination Polymers against Ammonia. *Chem. Eur. J.* **2014**, *20*, 15611–15617.